Chronic electrical stimulation of peripheral nerves via deep-red light transduced by an implanted organic photocapacitor

EJNEBY, M.; JAKEŠOVÁ, M.; FERRERO, J.; MIGLIACCIO, L.; SAHALIANOV, I.; ZHAO, Z.; BERGGREN, M.; KHODAGHOLY, D.; DEREK, V.; GELINAS, J.; GLOWACKI, E.

Nature Biomedical Engineering

2022, vol. 6, pp. 741-753

ISSN: 2157-846X

DOI: https://doi.org/10.1038/s41551-021-00817-7

Accepted manuscript

Nature Biomedical Engineering **volume 6**, pages741–753 (2022)

Chronic electrical stimulation of peripheral nerves via deep-red light transduced by an implanted organic photocapacitor

Malin Silverå Ejneby,[1,2] Marie Jakešová,[1,3] Jose J. Ferrero,[4] Ludovico Migliaccio,[1,2,3] Ihor Sahalianov,[1] Zifang Zhao,[6] Magnus Berggren,[1] Dion Khodagholy,[6] Vedran Đerek,[1,2,7*] Jennifer N. Gelinas,[4,5*] Eric Daniel Głowacki[1,2,3*]

[1] Laboratory of Organic Electronics, Campus Norrköping, Linköping University, SE-60174, Norrköping, Sweden
[2] Wallenberg Centre for Molecular Medicine, Linköping University, SE-58185, Linköping, Sweden
[3] Central European Institute of Technology, Brno University of Technology, Purkyňova 123, 61200 Brno, Czech Republic E-mail: eric.daniel.glowacki@ceitec.vutbr.cz
[4] Institute for Genomic Medicine, Columbia University Medical Center, 701 West 168th Street, New York, NY 10032, USA
[5] Department of Neurology, Columbia University Medical Center, New York, NY 10032, USA E-mail: jng2146@cumc.columbia.edu
[6] Department of Electrical Engineering, Columbia University, New York, NY 10027, USA
[7] Department of Physics, Faculty of Science, University of Zagreb, Bijenička c. 32, 10000, Zagreb, Croatia E-mail: vdjerek@phy.hr

Abstract: Implantable devices for the wireless modulation of neural tissue need to be designed for reliability, safety and reduced invasiveness. Here we report chronic electrical stimulation of the sciatic nerve in rats by an implanted organic electrolytic photocapacitor that transduces deep-red light into electrical signals. The photocapacitor relies on commercially available semiconducting non-toxic pigments and is integrated in a conformable 0.1-mm3 thin-film cuff. In freely moving rats, fixation of the cuff around the sciatic nerve, 10 mm below the surface of the skin, allowed stimulation (via 50–1,000-μs pulses of deep-red light at wavelengths of 638 nm or 660 nm) of the nerve for over 100 days. The robustness, biocompatibility, low volume and high-performance characteristics of organic electrolytic photocapacitors may facilitate the wireless chronic stimulation of peripheral nerves.

Introduction

Implantable neural interfaces are at the heart of bioelectronic medicine, a growing field which aims to provide electrical solutions to medical problems[1–3]. Direct electrical actuation of the nervous system is utilized clinically in deep brain stimulation[4], prosthetic retina implants[5], vagus nerve stimulation for treatment of epilepsy[6] and other disorders[7,8], as well as in numerous other applications. Meanwhile, the list of emerging technologies at a preclinical phase is constantly growing[9,10]. Several fundamental engineering hurdles need to be overcome to facilitate widespread implementation of bioelectronic devices and ensure optimal clinical outcomes[11,12]. A key challenge is to improve long-term powering and miniaturization of implantable devices, motivating exploration of methods to wirelessly actuate and control implants from outside of the body. The most common approaches involve radio frequency (RF) power transmission or electromagnetic induction[13]. Although

these technologies are being developed for clinical use[11,14–16], RF imposes size and shape constraints for transmitting and receiving components. The volume of the receiver (implanted inside the body) ranges from 30-600 mm^3,[17] including antennae for RF transmission, electrodes for nerve stimulation, and device packaging for protection of rigid Si-based electronics from body fluids. Efficient RF coupling and tissue heating are also factors that limit clinical translation.[17] An alternative emerging approach leverages acoustic waves at ultrasound frequencies. Ultrasonic energy can be used to stimulate nervous tissue directly[18] or can be absorbed by piezoelectric transducers to power devices[19]. Though very promising, due to acoustic impedance matching requirements the ultrasound transmitter must be in intimate contact with the skin, and penetration through layers of different tissues can be a limitation of ultrasound technologies. Overall, there is a strong demand for fully implantable systems which require less anatomical space than the aforementioned approaches, and which are minimally-invasive, remotely-powered, and easy to use.

Optical power transfer has been proposed as an alternative approach[20,21]. In this work, we hypothesized that tissue-penetrating deep-red light (620-800 nm) could effectively control and power implants wirelessly without requiring rigid or bulky implanted components. Four main features support this idea. Firstly, deep-red wavelengths occupy a "tissue transparency window" of the electromagnetic spectrum. This is due to the fact that absorbance spectra of both biopigments in the body and water have local minima in this region of the spectrum. As a consequence, light in the 620-800 nm region has relatively good penetration depth in skin, muscle, and fat tissue[22]. Next, light-emitting diode (LED) technologies are well-established and mature. High brightness, efficient LED light sources are reliable and commercially available in huge variety and at low cost. Third, light-based technologies are widely-accepted in medical practice, in therapeutic and imaging applications. Lastly, devices relying on optical power transfer can easily be made on the sub-millimeter scale (<1 mm^3), thanks to the availability of relatively efficient and easily-processable thin-film photovoltaic materials. Deep-red light could therefore address the challenge of making small-scale devices that can be actuated and controlled wirelessly from outside the body.

The combination of an optoelectronic transducer implant and deep-red light has been less explored than other power transfer methods, though several promising examples exist[20]. Recent efforts have been reported to make light-powered/rechargeable pacemakers[23,24]. Pioneering work on inorganic photovoltaic stimulators demonstrated acute *in vivo* efficacy for spinal cord stimulation, which relied on power transfer through ≈3 mm of tissue[25]. Recently, flexible on-skin LED arrays have been shown to accomplish efficient optical power transfer to implanted photovoltaic arrays based on GaAs. Such arrays were demonstrated to recharge batteries of an implanted stimulator[21]. On the other hand, a variety of approaches in basic and biomedical research use light to mediate neurostimulation due to its noninvasiveness and versatility[26–28]. Optogenetics endows cells with light responsiveness[29], but the necessity of genetic manipulation to accomplish this is not always facile or desirable for many applications, and remains a controversial proposition for clinical translation. Moreover, few opsins are available with light sensitivity in the red part of the spectrum[30]. These observations have spurred exploration of other ways to use light to interface with the nervous system over the past decade. Photothermal heating with light can be used directly to trigger a thermocapacitive effect, stimulating neurons *in*

vitro[31]. To better control specificity and localization of this approach, light-absorbing nano or microparticles can be used as photothermal mediators[32]. Both inorganic[33] (primarily silicon)[34] and molecular[35] or polymeric[36] semiconductors can be used as light absorbers for various *in vitro* stimulation demonstrations. Nanoscale silicon biointerfaces can be tuned to provide highly-localized photocurrent stimulation in single cells[28]. Few of these concepts have proven scalable or reliable for *in vivo* settings, and chronic deployment remains elusive. To-date, photovoltaic neurostimulation has been developed for retinal protheses, based on arrays of silicon[37] or organic semiconductors[38]. Highly optimized silicon diode-based technologies for retinal stimulation[39,40] have advanced to clinical trials. Delivery of light is straightforward for intraocular applications. Getting sufficient light to devices implanted below skin and other tissues, however, is not as obvious. We propose that using organic semiconductors as the active optoelectronic component could facilitate light-mediated neurostimulation for such applications[41] due to high absorbance coefficient (10-1000 times greater than Si), mechanical flexibility, and biocompatibility[42]. They can enable ultrathin and minimally invasive form factors inaccessible in traditional inorganic materials. Such approaches to noninvasive photostimulation of the nervous system *in vivo* have not yet been demonstrated.

Our biointerface devices use commercially available organic pigments[35,43], which belong to the category of safe and nontoxic colorants approved for a wide range of consumer products like food colorants and cosmetics[44]. Their nontoxicity originates from their non-bioavailability, which in turn is caused by complete insolubility and their formation of stable crystals. The specific pigments we use, phthalocyanine and rylene diimide pigments, have a low-energy molecular structure based on aromatic carbon-nitrogen heterocycles. These intrinsically robust molecular motifs are further stabilized by strong intermolecular interactions mediated by π-π stacking and hydrogen-bonding. These forces lead to the formation of organic pigment nanocrystals which have, aside from favorable electronic properties, outstanding stability in aqueous environments. For these reasons, we postulate that this class of organic materials may be suitably resistant to degradation to enable stable *in vivo* interface devices. These pigment materials form the basis of our recently-developed organic electrolytic photocapacitor (OEPC)[45]. This device employs a nanocrystalline donor-acceptor PN junction acting as the charge-generating element and primary stimulation electrode, which is surrounded by a concentric return electrode. The stimulation efficacy of this minimalistic device architecture was validated for cultured neurons and explanted retinal tissues[45]. More recently, the capacitive charging behavior was characterized on the single-cell level, accompanied by direct electrophysiological measurement of the device's impact on voltage-gated ion channels[46,47]. These *in vitro* demonstrations were based on rigid OEPCs. Here we integrate the OEPC into an ultrathin flexible architecture suitable for chronic *in vivo* implantation. The photoelectrical charging behavior of the OEPC stimulation devices effectively activated the rat sciatic nerve *in vivo* and enabled precise control of stimulation by varying light intensity and pulse duration. We fabricated the OEPC into a self-locking ultrathin cuff that was simple to surgically place and immobilize inside a freely-moving animal over months. Deep-red light delivered through the skin surface to the implanted OEPC evoked compound muscle action potentials (CMAPs)[48] via sciatic nerve stimulation at an operation depth of approximately 10 mm. Device implantation did not impede physiologic motor behaviors, and devices maintained their operation for up to 3 months after implantation.

With a total volume of 0.1 mm^3, OEPCs are the lowest-volume wireless peripheral nerve interface reported to-date[17]. These results suggest that OEPCs provide a viable approach to chronic *in vivo* neurostimulation, and hold potential for translation to clinical applications.

Results

Design and fabrication of flexible OEPC nerve stimulators

Our approach to wireless neurostimulation leverages organic molecular thin-films to efficiently transduce light impulses into electrolytic currents that modulate activity of excitable cells. As in our *in vitro* studies leading up to the present work[45,46], we rely on the phthalocyanine (H_2Pc, P-type) / *N,N'*-dimethyl perylenetetracarboxylic bisimide / (PTCDI, N-type) heterojunction to create OEPCs (Figure 1a). The bilayer is deposited by thermal vacuum evaporation to form a densely-packed film of nanocrystals (Figure 1b). This PN junction combination has high reliability and stability in aqueous environments. To transform the OEPC into an implantable device capable of efficiently delivering stimulation current, we integrated it into a ribbon-like structure that can conform around the nerve. We used thin (5 μm) parylene C, a well-established biocompatible polymer, as a substrate material[49]. The first design challenge we faced was producing a semitransparent conducting back electrode layer on the substrate. A key materials selection criterion is semitransparency of this underlying conductor, to allow light to reach the absorbing PN semiconductor layer. We utilized thin thermally-evaporated Au (10 nm thickness) due to its excellent conductivity, good transparency, and mechanical flexibility[45]. In the OEPC architecture, the back conductor functions as a return electrode, providing a completion of the current path generated by the PN junction. The PN junction, upon illumination, will produce an electrolytic double layer as electrons accumulate at the N-type material/electrolyte interface. Meanwhile, holes are driven into the underlying metallic conductor, creating an oppositely-charged double layer around the PN pixel thus giving rise to ionic currents around the device (I_{ionic}, Figure 1c). From the point of view of an underlying nerve, this device architecture produces a tripolar-type stimulating electrode arrangement (Figure 1c inset)[12]. These materials were integrated to ultimately fabricate chronically implantable photocapacitors (CIPs) for testing in an animal model. We placed these devices on rat sciatic nerve intra-operatively, and subsequently implanted them for long-term *in vivo* evaluation (Figure 1d). During chronic photostimulation, 638 nm light impulses would need to be beamed through about 10 mm of tissue to drive the CIP (Figure 1e). We first sought to investigate the feasibility of this approach – can light be transmitted efficiently and safely to reach a device located below the surface of the skin? Light propagation through different tissues has been studied in detail[22]. We applied established numerical Monte Carlo (MC) methods[50,51], and used known optical constants for rat tissue[52] to determine that a conventional 700 mW laser diode at 638 nm will deliver light intensities in the range of tens of mW/cm^2 at a depth of 1 cm (Figure 1f). It is also critical to consider the light power safety. To first order, in all experiments in this work we have set a limit to light doses to a maximum of ten times below the accepted laser safety standards for skin exposure according to the *American National Safety Standard for the use of Lasers*[53], according to which maximum permissible exposure for skin is 195 mJ/cm^2. With a 700 mW laser diode on a 4 mm^2 area, a 1-ms pulse yields 17.5 mJ/cm^2. To

understand the magnitude of photothermal effects, we combined our MC calculations with finite-element methods, to construct a heat-dissipation model for light impinging on live rat tissue (see Supplementary Appendix 1: *Calculation of Photothermal Heating*). From this model it emerges that if relatively high light powers (~1 W) are delivered over relatively short periods of time (≤ 1 ms), the total dissipated heat is negligibly low, causing a temperature increase on the order of a thousandth of a degree. Heat is transferred differently in the various tissue layers, with the largest relative change appearing at the surface of the skin. The largest photothermal change is 0.005°C, with the longest illumination time of 1 ms. Further, we find no evidence for photothermal effects on neural tissue when operating these devices *in vivo* (see Figure 3).

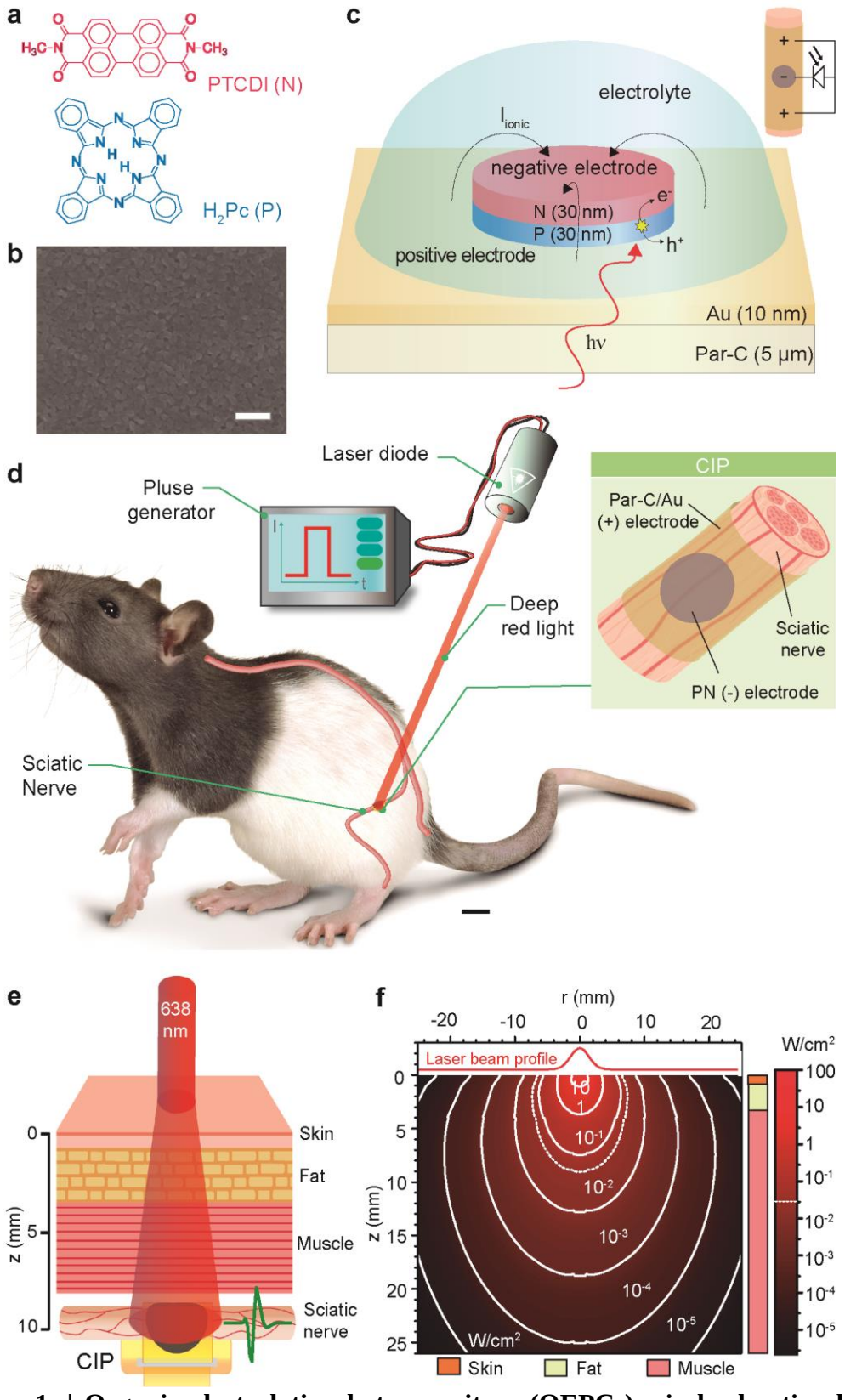

Figure 1. | Organic electrolytic photocapacitors (OEPCs) wirelessly stimulate the sciatic nerve *in vivo*. a, Molecular structures of the active components in the PN

semiconducting layer. Phthalocyanine (H_2Pc) functions as the light-absorbing and electron-donating P-type layer. *N,N'*-dimethyl tetracarboxylic diimide (PTCDI) acts as the electron-accepting N-type layer and forms an electrolytic contact with the surrounding electrolyte. **b,** The sequentially evaporated PN bilayer (30+30 nm) forms a compact thin film featuring a distinctive nanocrystalline morphology apparent in scanning electron microscopy. Scale bar 200 nm. **c,** Diagram of the OEPC device and its operating principle. The PN bilayer is processed on top of a semitransparent gold film (10 nm), which acts as the return (+) electrolytic contact. Light in the deep-red region (638 or 660 nm) is used for excitation of the P-type layer. Photogenerated electrons travel through the N layer to accumulate at the electrolyte interface, forming an electrolytic double layer. Concurrently, holes are driven from the P layer into the underlying gold, forming an oppositely-charged double layer. During charging of the device (beginning of light pulse), and discharging, (end of light pulse), ionic displacement currents (transient ionic current, I_{ionic}) flow around the device and thus through surrounding tissue. This produces biphasic stimulation pulses. The inset shows how the OEPC, understood simply as an illuminated photodiode, couples to a nerve with a quasi-tripolar arrangement. **d,** Schematic of the *in vivo* implanted OEPC photostimulation experiments performed in this study. Scale bar 1 cm. The inset details how a chronically-implantable photocapacitor (CIP) cuff is placed around the nerve, with the configuration of the primary PN photoelectrode (-) with the surrounding (+) return electrode. **e,** Following implantation, deep-red light penetrates through skin, fat, and muscle tissues to reach the OEPC, located at a depth of roughly 10 mm. **f,** Numerical calculation of penetration of a stimulating red light beam through simulated animal tissue layers, showing the effectiveness of 638 nm light to access the implanted OEPC. The dotted white line represents the cross-sectional region with 50 mW/cm^2 of intensity.

Photoelectrical characterization

While stimulation electrode benchmarking methods are well-established[54,55], determining relevant parameters for an electrically-floating photoelectrode device requires special consideration. A common figure of merit for a neurostimulation electrode is the electrolytic charge density that the electrode can inject, or charge density per phase[54]. In order to measure this parameter in the case of OEPCs, we devised the electrophotoresponse (EPR) method[46] (Figure 2a). In EPR, the photovoltage or photocurrent is registered by contacting the back electrode (Au) with a probe and measuring versus an ideally nonpolarizable electrode (Ag/AgCl) immersed in an electrolyte. This electrolyte is confined to the top of the PN semiconductor region. The device is illuminated with light pulses from the bottom, through the semitransparent gold film, thus mimicking the anticipated configuration during *in vivo* neurostimulation. The photovoltage to which the PN/electrolyte junction charges can be measured using an oscilloscope. Photocurrent is quantified in the same arrangement using a current amplifier. During a light pulse of 638 or 660 nm, the OEPC charges to around 300-320 mV and the capacitive displacement currents under the same conditions peak at around 2 mA/cm^2 (Figure 2b). The photovoltage in this configuration represents the thermodynamics of the PN junction band-edge in contact with the electrolyte. Most relevant to neurostimulation applications, the photocurrent measurement quantifies the charge that can be injected as a function of light intensity and pulse length. Dynamics are rapid, with maximum charging current peaking at 20 µs. In the context of OEPC devices, charge density can be modulated with light intensity and light pulse length. We plot the

charge density per phase as a function of light intensity (Figure 2c) and light pulse duration, from 50 µs to 1 ms (Figure 2d). The 638 nm wavelength was found to have slightly better photocharging efficiency relative to 660 nm. This finding corresponds to the absorption spectrum of the H_2Pc p-type absorber layer[45]. Importantly, both wavelengths are typical in readily-available LED illuminators.

While the EPR measurement allows quantification of photocharge density that the OEPC device can generate, it does not faithfully reflect the final operating conditions of an OEPC stimulator. *In vivo*, the OEPC device is electrically floating. The organic PN pixel forms an electrolytic closed circuit with the back electrode.[45,56] The displacement current which flows around the device during photocharging and discharging generates transient potentials in the solution which affect the electrophysiology of nearby cells, as established in our earlier *in vitro* studies[46,47]. To visualize this effect, we measure the transient potential (V_T) above the PN pixel in electrolyte (Figure 2e). The V_T was registered between a recording microelectrode positioned at 1 mm above the center of the PN pixel versus a distant reference electrode. Consistent with the PN polarity of the OEPC, illumination resulted in a cathodic transient voltage peak followed by an anodic transient when the light was turned off and electronic charge carriers recombine (Figure 2f inset). This voltage transient corresponds temporally to the electrical perturbation that adjacent axon bodies will experience. It mimics a charge-balanced biphasic stimulation protocol, which is typically used to avoid tissue and electrode damage during neurostimulation[57,58]. The actual transmembrane potential induced will vary based on the position and distance from the stimulating electrode[46,59]. The magnitude of the V_T was directly proportional to the size of the PN pixel, ranging from around 8 mV for a 1 mm diameter PN pixel to 30-40 mV for a 3 mm diameter pixel (Figure 2f). Taken together, these results demonstrate the operating mechanism and parameters for OEPC-mediated neural stimulation and highlight the importance of PN pixel size as a key parameter governing effectiveness of neuromodulation.

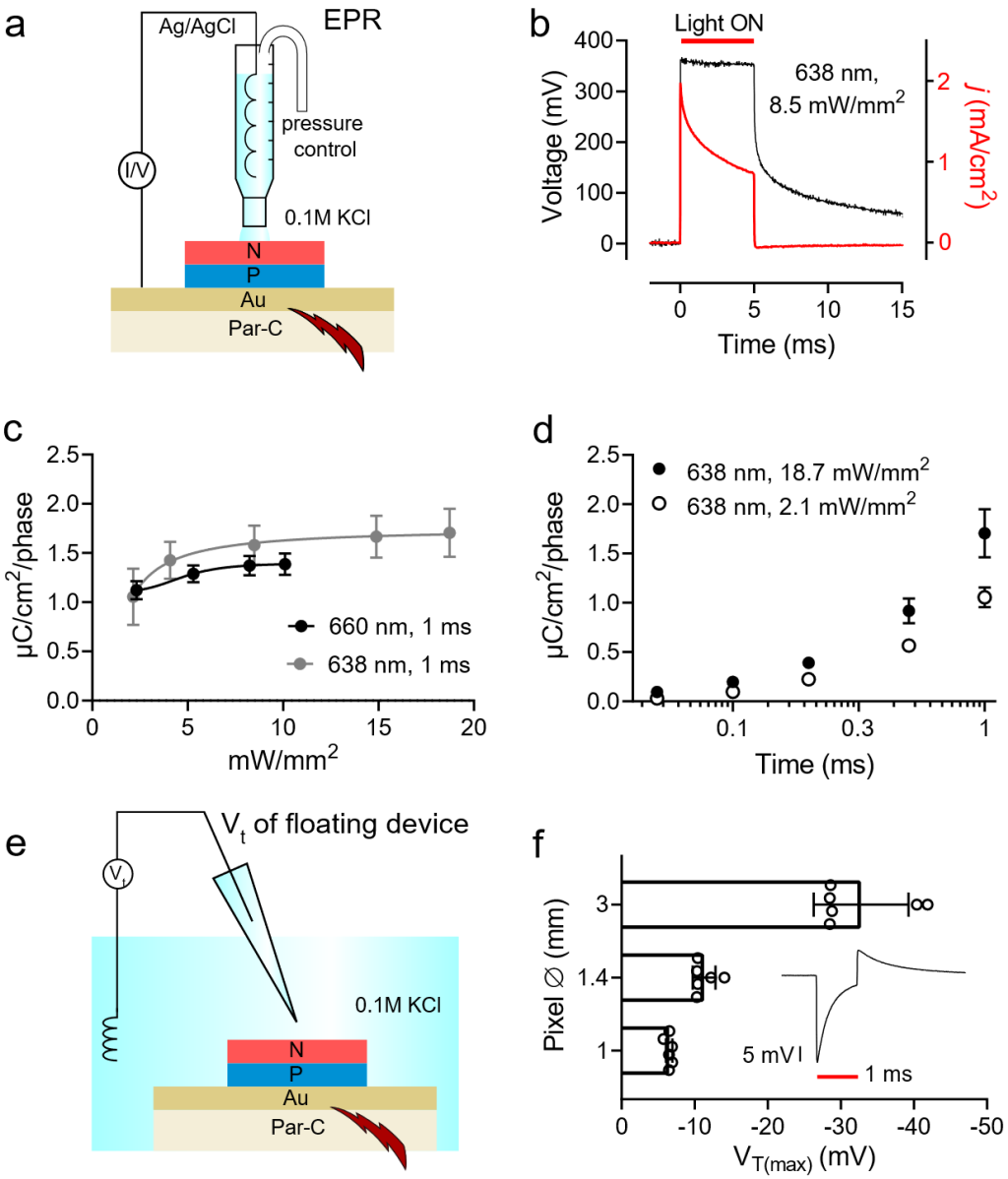

Figure 2. | Photostimulated OEPC devices deliver rapid localized electrolytic pulses **a,** Schematic of the electrophotoresponse (EPR) closed-circuit measurement, where photovoltage or photocurrent is measured between the bottom metal contact and an electrolytic contact. This method probes photogenerated charge injection across the PN/electrolyte junction, and photovoltage reflects the energy levels of the metal/PN/electrolyte stack. **b,** Photovoltage and photocurrent registered by EPR, using excitation with a 638 nm laser diode. **c,** Charge density per phase as a function of light pulse intensity, for 1 ms light pulses of either 638 or 660 nm light, n=8, ±SD. **d,** Charge density per phase as a function of light pulse duration, n=8, ±SD. **e,** Transient voltage, V_T, probes the voltage perturbation generated in electrolyte when displacement currents flow from anode (Au) to cathode (PN). V_T is registered between a point above the center of the PN pixel versus a distant Ag/AgCl reference. This method reflects the actual electrical

perturbation nerve fibers would experience from the OEPC stimulator. **f,** V_T during a 1 ms light pulse, showing the clear biphasic current behavior. All pixels give qualitatively the same trace, only the magnitude of voltage varies with pixel diameter. The bar graph plots the cathodic maximum V_T as a function of PN pixel diameter. 638 nm, 17.5 mW/mm^2 intensity used. n = 3 devices for each size, each measured two separate times ±SD.

Acute validation of light-induced nerve stimulation

To test the efficacy of *in vivo* neuromodulation using OEPC devices, we used the well-established rat sciatic nerve model[12,16]. To determine the effectiveness of OEPC-mediated nerve stimulation, microwires capable of measuring evoked compound muscle action potentials (CMAPs) were placed in biceps femoris (Figure 3a) and plantar muscle groups (Supplementary Figure S1) of 5 rats. OEPC devices integrated into parylene C ribbons were wrapped around the nerve with the PN pixel immediately adjacent to the epineurium. The ribbon was not fixed in any way other than simple adhesion of the loose plastic ends to each other via capillary interactions in the presence of water. Intra-operatively, OEPC ribbons with differently sized PN pixels (1 mm ø, 1.4 mm ø, and finally 3 mm ø, denoted henceforth as three device sizes S, M, and L) were illuminated using an LED (660 nm) with a collimator lens that was placed above the exposed nerve (Figure 3b). OEPCs were consistently placed such that the PN pixel pointed in the dorsocaudal direction relative to the rat's body. To ensure that any recorded CMAPs were the result of light-mediated photovoltaic stimulation, we conducted experiments with two types of sham devices: a bare parylene C covered with Au, and a device with a photothermal absorber layer, "thermal control", TC (Figure 3c). Illumination of the Au sham device did not yield any response or artefact (Figure 3d, Supplementary Figure S1b). This indicated that light impulses alone were not eliciting any stimulation. To evaluate the possibility of photothermal heating, however, it was necessary to add a layer that would absorb light and locally generate heat. For this purpose, we deposited thin films of indigo pigment, which has optical absorption closely mimicking that of the active PN layer. Indigo dissipates 99%+ of absorbed light as heat[60]. We found that these photothermal control samples likewise produced no electrophysiological response (Figure 3d). This allows us to rule out photothermal stimulation effects. In contrast, illumination of OEPC devices did reproducibly stimulate the sciatic nerve, as demonstrated by visually observable twitching in sciatic-innervated muscles and recorded CMAPs (Figure 3e: CMAPs in response to 1-ms, 9.4 mW/mm^2, illumination pulses; see also Supplementary Figure S1c, and Supplementary Video 1). Increased size of the PN pixel strongly correlated with higher stimulation as measured by larger amplitude of both observable movement and the average CMAP waveform (Figure 3e, Supplementary Figure S1c), concurring with the predictions of V_T measurements (Figure 2f). The elicited CMAPs were also highly consistent in both amplitude and latency after repetitive light-stimulation (Figure 3f, Figure S1d; 25 light-pules, 3 seconds between). Taken together, these results demonstrate the ability of the OEPC to transduce light impulses to electrical potentials that are capable of consistently and repetitively stimulating the sciatic nerve, with response magnitude dependent on PN pixel size.

In vivo neurostimulation often requires precise control of response timing and amplitude. Using M- and L-sized OEPC devices, we therefore determined the relationship between light intensity and light pulse duration with CMAP responses (Figure 3g-i, Figure S1e-h).

CMAP responses were quantified using the amplitude of the M-wave. The H-wave was detected for a subset of stimulations, namely those with a relatively low charge dose, close to the threshold for a visible movement (Figure S1f). For size M devices, light intensities in the range of 4-10 mW/mm^2 evoked robust CMAP responses, and visible movements in the leg and paw (Figure 3g,h, Figure S1e,g). Light-pulse durations between 200-500 µs were needed to reach a threshold of visible movement. With the L-sized OEPC device, the light intensity and light-pulse duration could be significantly reduced (Figure 3g,i; Supplementary Figure S1e,h). For instance, at 1 mW/mm^2, using 1-ms light-pulses, the CMAP response already saturated for both muscles (Figure 3i, Figure S1h). Consequently, shorter light-pulse lengths (100 µs) could be used to reach a threshold of visible movement. Therefore, light intensity, light-pulse duration, and PN pixel size interplay to produce a given level of OEPC-mediated neurostimulation.

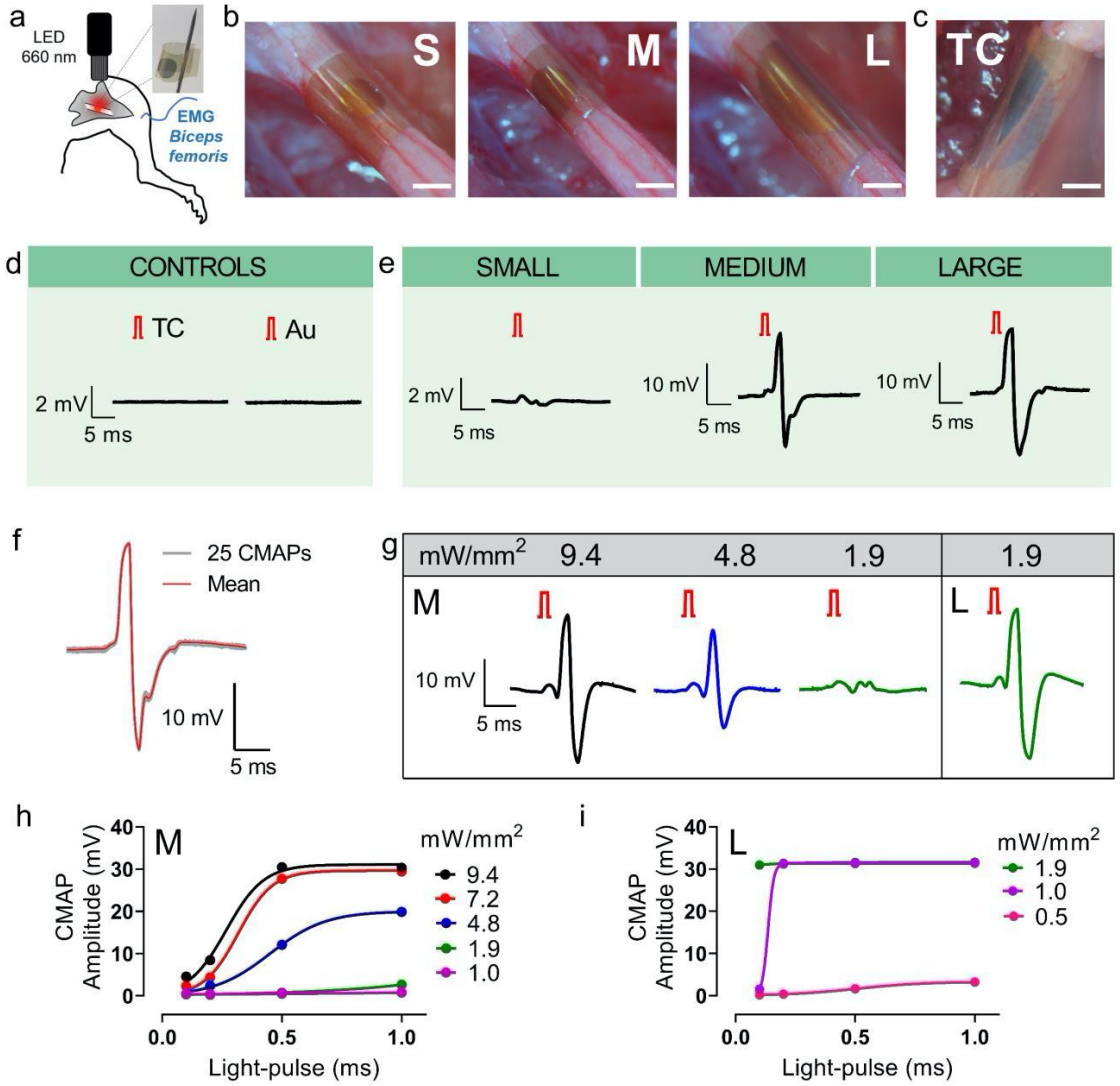

Figure 3. | Acute sciatic nerve photostimulation is precisely controlled by varying OEPC device size, light intensity, and stimulation pulse length. a, Schematic of the sciatic nerve stimulation experiment design for acute conditions, with inset photograph

showing a free-standing device prior to implantation. **b,** Photographs of S, M, and L devices wrapped around the sciatic nerve. Scale bar 1 mm. **c,** An L-sized thermal control (TC) sham, consisting of a pixel of indigo, a pigment which efficiently heats up but does not generate charge. **d,** Illumination of sham devices, only Au on parylene C (Au), or the indigo thermal control (TC), gives no response or artefact. 1-ms light-pulses, 9.4 mW/mm^2 irradiation. **e,** Averaged evoked CMAPs in the biceps femoris (Rat #1) during 25 repetitive light-pulse stimulation (1 ms pulses, 9.4 mW/mm^2 irradiation, 3 seconds in-between), for the respectively-sized OEPC devices. **f,** Highly reproducible repeated stimulation can be evidenced when 25 CMAPs are plotted on top of each other (in grey) for biceps femoris after repetitive stimulation with a M-sized OEPC device (Rat #1, 1 ms light pulses, 9.4 mW/mm^2 irradiation, 3 seconds in-between). The averaged response is shown in red. **g,** Examples of CMAPs evoked at different light intensities, 1 ms pulses on M- and L-sized OEPC devices (Rat #2) **h,** Average biceps femoris CMAP amplitudes versus light-pulse length, at different light intensities. M-sized OEPC device. 25 pulses, 3 seconds in-between, for each condition. **i,** Average biceps femoris CMAP amplitudes versus light-pulse length, at different light intensities. L-sized OEPC device. 25 pulses, 3 seconds in-between, for each condition. CMAP amplitude saturates at lower intensities and pulse times for the L device compared with the M device.

Chronically implantable photocapacitor (CIP) development and implementation

Following acute nerve stimulation experiments, we aimed to engineer the OEPC for chronic implantation by developing a more chemically and mechanically stable interface with the nerve. The OEPC relies on an ultrathin Au semitransparent conductive layer on parylene C as the return (+) electrode. However, we found that this Au layer loses conductivity and delaminates when stored in chloride-containing electrolytes for more than two weeks. This likely precludes *in vivo* longer-term use. To stabilize the thin Au, we deposited a 30 nm-thick encapsulating layer of indium tin oxide (ITO), which has excellent adhesion with Au[61]. ITO has a wide electrochemical passivity window[62], is biocompatible[63,64], and does not compromise transparency or conductivity. In the range of potentials and conditions we have used in our work, Au/ITO bilayers have suitable stability. Furthermore, the ITO layer enabled convenient new micropatterning approaches for us, based on the parylene peel-off lithography[65], as it served as an effective etch-stop for O_2-reactive ion etching (see *Methods*). ITO is used to protect the Au of the return electrode, while Au without ITO capping remains the contact metal to the PN layers. To predict *in vivo* stability and functionality of CIP devices, we conducted accelerated aging/stressing tests by immersing devices in 0.1 M KCl solution set to 42 ˚C, and illuminating them with constant light pulses (2 Hz) delivered through a high-density LED array. Devices were periodically removed and photovoltage and photocurrent were registered using the previously-described EPR technique. No devices failed, and photovoltage/current retained greater than 85% of starting values over the course of 89 days of continuous stressing (corresponding to 14 million charge/discharge cycles; Figure 4a). Thus, the ITO modification of the OEPC gives promising indications of robustness. Because the L-sized OEPCs performed optimally at low-light intensities in acute experiments, this PN pixel size was used for fabrication of CIP devices.

To ensure conformable contact with neural tissue and prevent damage caused by tension or pressure, we had chosen from the start to use ultra-thin parylene C substrates for the OEPC neural interfaces. Parylene C can maintain mechanical contact via capillary forces in the presence of water, but this contact was insufficient to immobilize the device on the nerve for long-term stable stimulation. Therefore, we adapted a parylene zip-tie locking mechanism[66,67] that allowed the device to form a cuff around the nerve in a fixated position. One end of the parylene C substrate ribbon was narrowed and modified to contain a small guiding loop, and the other end widened to contain a narrow locking loop (Figure 4b-d). When the guiding loop ribbon was passed through the locking loop, locking "teeth" along the lateral borders of the ribbon allowed for sizing of the cuff diameter and prevented slippage of the ribbon ends (Figure 4c). This CIP remained fully conformable, and was sized to accommodate the dimensions of rat sciatic nerve accessible through minimally invasive surgical incision. Evaporated aluminum, which is a relatively malleable metal, (1.5 μm thickness) encapsulated with parylene C, reinforced the loops and teeth (Figure 4e). These aluminum-stiffened "teeth" and loops provide mechanical robustness of the locking mechanism and enable facile manipulation with surgical tools during the implantation procedure.

Implantation was performed by sliding the ribbon of the CIP behind the sciatic nerve (Figure 4f) and pulling the guiding loop through the locking loop with fine forceps (Figure 4g). Once advanced through the locking teeth, the excess parylene C ribbon was trimmed and the sciatic nerve resumed anatomic position relative to the muscles of the hindlimb (Figure 4h). This procedure was straightforward and required 5 minutes of surgical time, fulfilling a key criterion for translation of such devices to practical applications[68]. The incision was then sutured, separating the CIP from the surface of the skin by approximately 10-15 mm of skin, subcutaneous tissue, and muscle (Figure 4i). Prior to the closure of the incision, CMAPs evoked by CIP devices had comparable light intensity-dependent amplitude responses to acutely implanted OEPCs, confirming that design modifications to enable chronic implantation did not adversely affect functionality (Figure 4j). It should be noted that the absolute amplitudes of the registered CMAPs are lower in the chronic implant conditions since we use on-skin electrodes rather than inserting microwires into the muscle tissue.

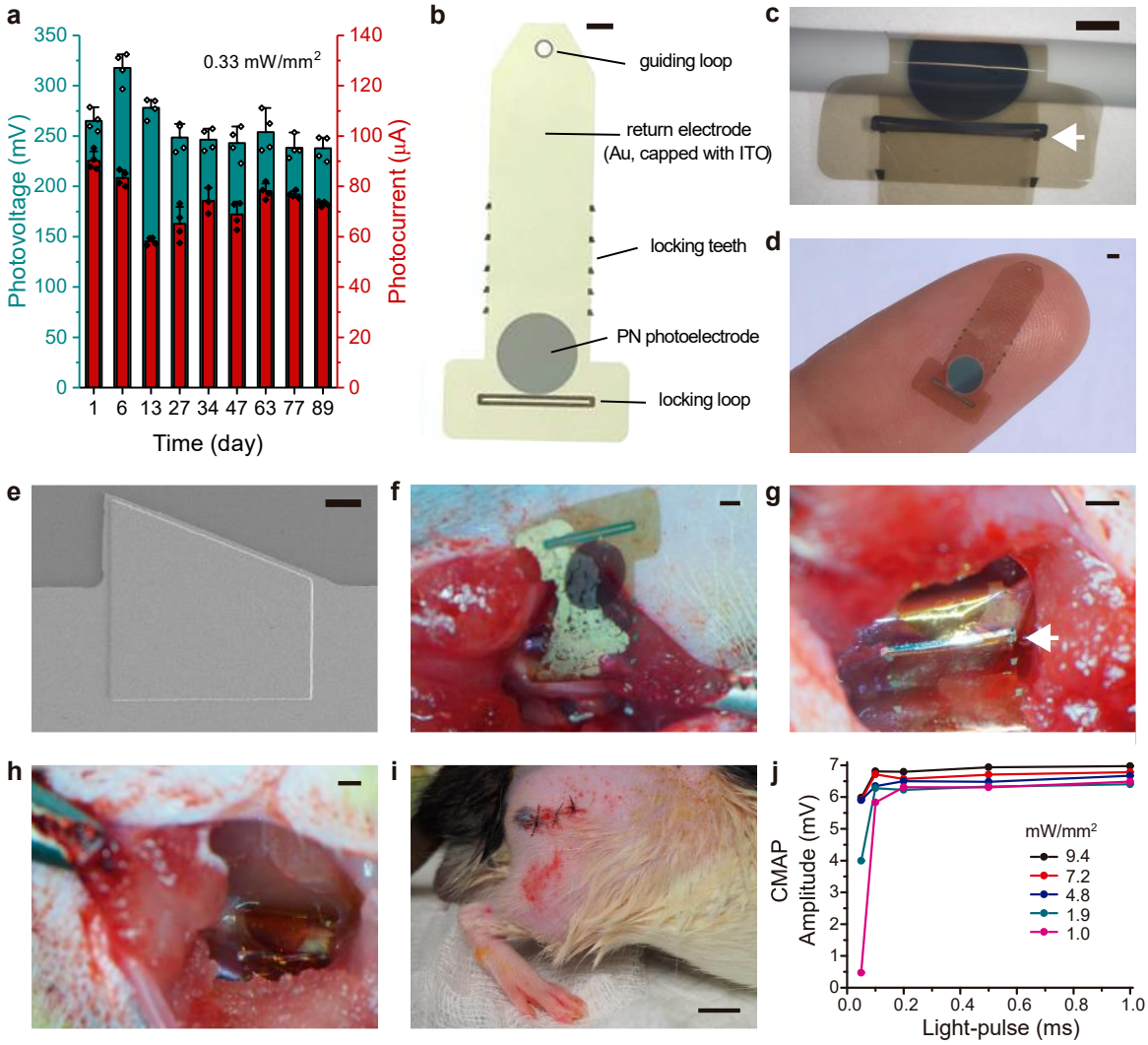

Figure 4. | Self-fixating OEPCs are mechanically robust to intra-operative placement and chronic *in vivo* implantation. a, Verification of *in vitro* stability: Photovoltage and photocurrent recorded periodically for devices subjected to accelerated aging conditions in 0.1 M KCl solution at 42 ˚C with light pulsing stress totaling 14 million charge/discharge cycles. n = 4, avg. ± SD. **b,** Photograph of the zip-tie CIP device with labeled components, and **c,** when wrapped and locked around a nerve phantom (1.4 mm diameter cylinder). The white arrow indicates the locking tooth. Scale bars 1 mm. **d,** Photograph of the conformable, ultralight and biocompatible CIP final design; scale bar 1 mm. **e,** SEM micrograph of the parylene-encapsulated aluminum tooth; scale bar 40 μm. **f,** CIP implantation was initiated by inserting the end of the ribbon behind the nerve and tucking it below the nerve; scale bar 1 mm **g,** The PN pixel was positioned adjacent to the external facing surface of the nerve and the end of the ribbon was pulled through the loop to lock the ratchet teeth against the loop edges (white arrow); scale bar 1 mm. **h,** CIP device closed around sciatic nerve, scale bar 1 mm. **i,** Sutured incision after CIP implantation was complete, scale bar 1 cm. **j,** Relationship between light intensity/pulse time (638 nm diode laser) and CMAP amplitude for implanted CIP device prior to incision closure.

We implanted CIP devices into a cohort of six rats and monitored functionality at regular intervals over the course of three months. To minimize animal discomfort, we recorded CMAPs through gel-based cutaneous electrodes (Figure 5a). Light stimulation from outside the body (using a 638 nm diode laser with a roughly 2×2 mm illumination spot, 700 mW max as shown in Figure 1d-f) elicited robust and repeatable CMAPs in all rats, some of which were associated with large-amplitude muscular twitches (Figure 5b, Supplementary Video 2).

CIP devices generated detectable CMAPs in all rats for 20 days, and at least half were functional for longer than 60 days (Figure 5c). In two rats, devices remained functional at timepoints greater than 100 days post-operatively, and CMAPs were obtainable in both the anesthetized and awake states (Figure 5d,e). Furthermore, when CIPs were functional, latency of CMAP onset from application of light stimulus was relatively constant for light stimuli of variable intensity and duration (Figure 5f), indicating stable nerve conduction velocity at values expected for the intact rat sciatic nerve[69]. We observed that CMAP amplitude was typically stable for a prolonged time period without decay, but could experience abrupt decrement (Figure 5d, left to middle) that was associated with slightly increased CMAP latency (Supplementary Figure S2). However, CIP devices remained capable of eliciting CMAPs with similar amplitude and latency to those obtained shortly after implantation when light intensity was increased by eliminating tissue attenuation (Figure 5d, right, Supplementary Video 3, Supplementary Figure S2). Given these results, we hypothesize that the alteration in CMAP properties during the implantation period was related to generation of a submaximal neural excitatory pulse due to decreased CIP stimulation performance (*i.e.* device degradation) rather than compromise of the nerve[70]. Post-mortem explantation of CIP devices revealed partial delamination of organic PN material from the parylene C substrate (Supplementary Figure S3). Partial delamination will render that part of the device unable to photogenerate current, thereby reducing stimulation efficacy. This is a possible degradation pathway. This observation of device degradation is in contrast to the results of the accelerated ageing tests *in vitro* shown in Figure 4a. These findings highlight the importance of performing chronic *in vivo* experimentation in order to subject devices to the full range of biochemical and mechanical stressors present in a freely moving organism.

The preserved conduction velocity values we observed during CIP implantation suggested that the device did not result in functionally relevant nerve damage. None of the rats demonstrated motor deficit at any time post-implantation, as all implanted rats were capable of running, standing on hindlimbs, and climbing. To further assess this notion, we performed quantitative behavioral testing in an additional cohort of rats (n = 7). Four rats underwent CIP implantation on one sciatic nerve and a sham surgical procedure on the contralateral limb. An additional three rats did not undergo any procedure and served as controls. Functional motor control was evaluated using a horizontal ladder task[71], with each hindlimb foot placement scored across experimental and control rats (Supplementary Video 4). We found no significant difference in the accuracy of hindlimb placement between CIP-implanted and -unimplanted hindlimbs in experimental rats (Figure 5l,m). Furthermore, comparison to the control cohort revealed no significant difference in task

performance, suggesting that CIP-implanted rats could not be distinguished from naïve animals in regard to motor function (Figure 5m). We also evaluated this cohort for indicators of CIP-related neuropathy using the von Frey test. Threshold for paw withdrawal was determined as per established protocols[72]. We found that the paw innervated by the CIP-implanted nerve did not have a consistently different threshold for paw withdrawal across rats (Figure 5n). There was also no significant difference in paw withdrawal threshold between the experimental and control rats (Figure 5o). These results indicate that CIP implantation does not result in neuropathy.

Furthermore, we did not observe gross pathological differences between CIP-implanted sciatic nerves compared with sham surgical control nerves, suggesting that the conformable nature of the device prevented structural injury (Figure 5g-h). Furthermore, there were no statistically significant different expression levels of neurofilament or GFAP between CIP-implanted nerves and sham controls (Figure 5i-k). Together, our functional, behavioral, and histological results support the preserved functionality of peripheral nerves chronically implanted with CIP devices.

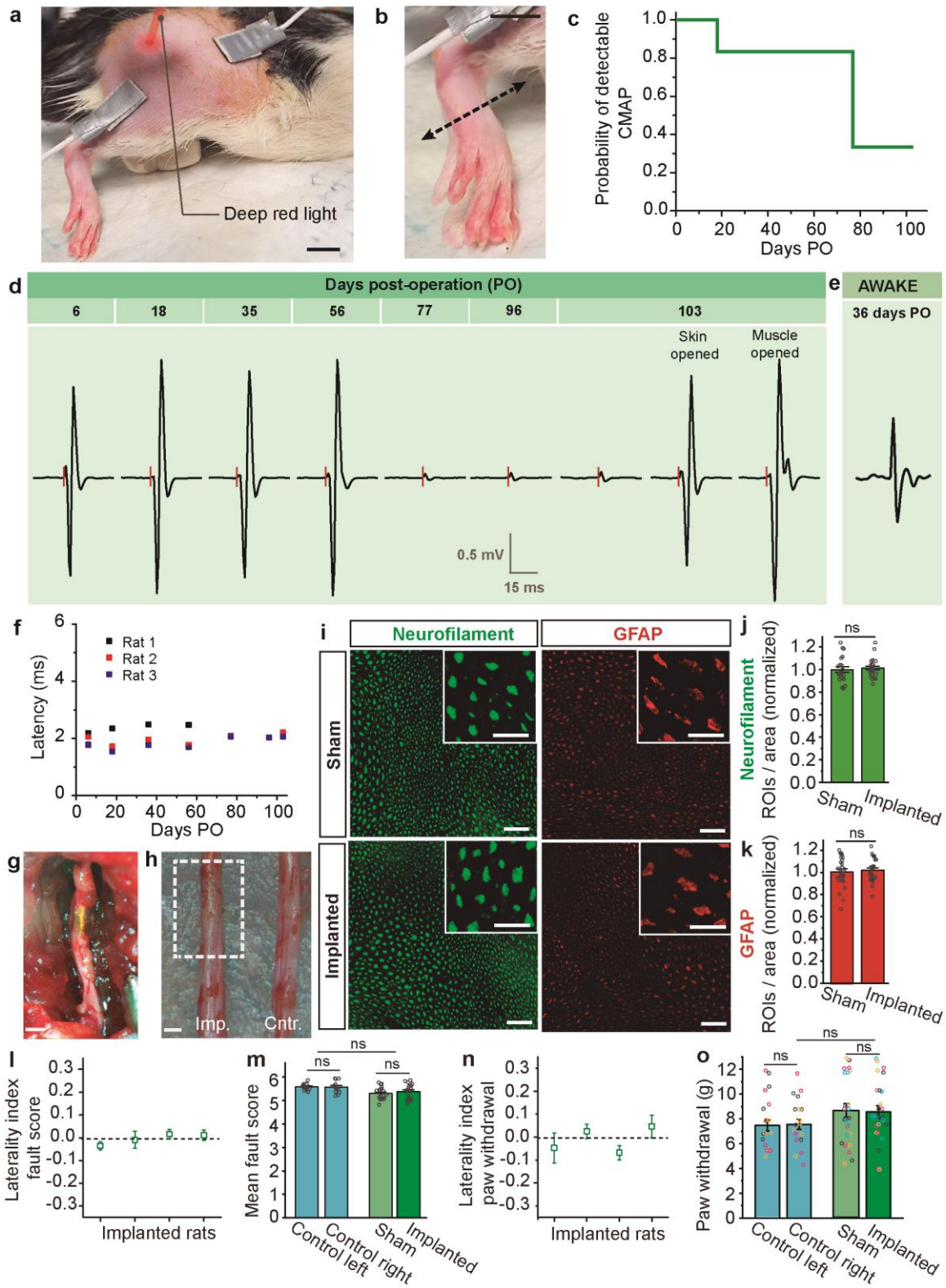

Figure 5. | OEPCs permit chronic, non-invasive *in vivo* sciatic nerve stimulation. a, Healed implanted area after post-surgical recovery with surface electrodes for EMG measurement attached; scale bar 1 cm. **b**, Photoinduced stimulation with 200-1000 µs at 700 mW induced observable muscular twitches; scale bar 1 cm; see Supplementary Video

2. **c**, Survival curve demonstrating the persistence of detectable CMAPs over the implantation period for all rats (n = 6). **d**, Representative averaged CMAPs over 103 days of chronic implantation. CMAP amplitude abruptly decreased by 77 days post-operatively (PO), but the device was revealed to be functional upon increased light delivery accomplished by opening the overlying tissue. The red dashes indicate light stimulation pulses. **e**, Representative photoinduced CMAPs recorded in an awake rat. **f**, Stable average latency between light pulse and CMAP peak over initial implantation period for the three rats with functional devices exceeding 60 days. **g**, Sciatic nerve implanted with CIP device (69 days PO); scale bar 3 mm. **h**, Implanted sciatic nerve after 103 days PO (Imp.) did not show gross pathological changes compared to the unimplanted contralateral sciatic nerve (Cntr.); scale bar 1 mm. **i**, Representative images of neurofilament and GFAP immunofluorescence (scale bar 20 μm) of transverse sections from OEPC-implanted and sham sciatic nerves (harvested 49-69 days post-operative); insets show higher magnification images (scale bar 10 μm). **j**,**k**, Quantification of number of immunopositive ROIs per area, normalized to the respective sham samples value, for neurofilament (n = 21/25 samples for sham/implanted sciatic nerves, 3 rats; p = 0.64) and GFAP (n = 25/26, 3 rats; t-test, p = 0.63); ns = not significant. **l**, All rats demonstrated similar hindlimb foot placement accuracy on the horizontal ladder task comparing sham and OEPC-implanted limbs (22-28 days PO, n = 97, 52, 135, and 132 steps for 4 rats). **m**, Hindlimb placement score on horizontal ladder task averaged between trials for control (n = 14 trials, 3 rats) and sham/OEPC-implanted (n = 19 trials, 4 rats) groups; ns = not significant (ANOVA, Bonferroni post hoc test; control, p = 1; implanted, p = 0.69; control vs implanted p = 0.72). **n**, von Frey testing revealed that OEPC-implanted limbs did not exhibit a consistently different threshold for paw withdrawal (22 to 34 days PO, n = 6, 7, 5 and 5 and trials for 4 rats). **o**, 50% threshold withdrawal response as calculated from von Frey testing for hindlimbs of control (n = 18 trials, 3 rats) and sham/OEPC-implanted (n = 23 trials, 4 rats) groups; different colors represent data from individual rats; ns = not significant (ANOVA, Bonferroni post hoc test; control/implanted/control vs implanted, p = 1). All error bars signify ±SEM.

Discussion

We have demonstrated that ultrathin organic photocapacitors can be microfabricated into conformable devices that generate sufficient electrical charge to modulate neural tissue *in vivo*. Device-mediated neuromodulation is accomplished via noninvasive, tissue-penetrating deep-red light. Chronically implanted photocapacitors exhibit physiologic stability and functional stimulation of a peripheral nerve over months in a freely-moving animal and do not incur motor deficit. In contrast to many other wireless neuromodulation devices, such as electromagnetic induction or ultrasound-based transducers, photocapacitors are microfabricated in a thin film configuration, resulting in a minimally invasive interface with tissue.

Photocapacitors offer several advantages compared to other stimulation modalities. Conventional electrical stimulation is accomplished by wired leads connected to an implanted power source, a configuration that is a common cause of device complications[73]. We show that photocapacitors are capable of chronic electrical stimulation by directly

converting light impulses into charge-balanced biphasic electrical signals, which is considered favorable for safe long-term stimulation[57]. Furthermore, the charge generated, and thus the neural response elicited, are directly related to the strength and duration of the light pulse. These features enable precise temporal and amplitude control of stimulation patterns. We have detailed how materials can be tailored to yield an ultrathin stimulator. First, robust and stable transparent conductors were optimized based on Au and ITO bilayers, which were engineered to stick reliably to the biocompatible polymer parylene C. Second, PN stimulation pixels are designed to efficiently deliver stimulation currents while keeping the absorbing layers at 60 nm of total thickness. Our work demonstrates that a conductor/semiconductor device layer combination with such low thickness can give robust photovoltaic stimulation. Because photocapacitors are microfabricated, they are inherently customizable. The size, configuration, and location of PN junctions can be modified within a variable shape and size of ribbon substrate, permitting application to nerves of different diameters, as well as other types of neural tissue. Our flexible locking mechanism minimizes risk of tissue damage while maintaining steady device position *in vivo*. The combination of this fixing mechanism with the concentric arrangement of the charge-generating PN pixel and the return electrode allows all the current to be directed into the nerve. In addition, no power source apart from the light pulse is necessary to operate the device, eliminating risks associated with implanted power hardware[74]. Photovoltaics based on the same active components as used in CIPs could also conceivably be used to non-invasively power other electrical components and enable information transmission via narrow-band LEDs and photodiodes.

To facilitate translation of photocapacitor devices to clinical applications, sustained performance should be demonstrated over prolonged time periods. Current CIP devices functioned for months in a freely moving rodent, and were not associated with detrimental behavioral or histological changes. There are three clear areas for optimization of CIPs: device stability, efficiency, and higher light sensitivity at longer wavelengths. Device longevity could be improved by encapsulation of the PN pigment with a conductive layer that prevents exposure of the internal device layers to electrolyte without decreasing electrical performance. The second parameter to optimize is light-to-charge efficiency of the devices, which would allow for operation in deeper tissues and increase the variety of targetable neural structures. Alternatively, it is possible to microfabricate conformable circuits that transmit electrical charge to deeper structures while maintaining the photoactive pigments closer to the external tissue interface for effective light activation. In terms of increasing the implantation depth for these technologies, much can be gained by tuning the stimulation wavelength. According to our MC model, a wavelength of 700 nm would be optimal in terms of transmission, and would nearly double the possible implantation depth (Supplementary Figure S4). On the other hand, tuning photocapacitor devices to respond even further to the red, 800-900 nm, could also be advantageous for comfort of human subjects, as at these wavelengths tissue transparency is sufficient for device operation, but human vision is no longer sensitive[39].

Electrical neurostimulation is employed not only to assay neural function in experimental paradigms[75], but is an efficacious and well-tolerated therapy for multiple neurologic disorders, from chronic pain to epilepsy[76]. CIPs can facilitate testing of such

neuromodulatory protocols in small animal models by minimizing device footprint and allowing for full device implantation without any tissue traversing elements, features that have been demonstrated to improve experimental outcomes[77,78]. The unique features of CIPs also advance the potential for translation to bioelectronic devices that require safe, long-term neurostimulation to treat pain and enable motor rehabilitation in humans.

Methods

OEPC device fabrication. H_2Pc, (Phthalocyanine, Alfa Aesar) and PTCDI (*N,N′*-dimethyl-3,4,9,10-perylenetetracarboxylic diimide, BASF) were first purified by threefold temperature-gradient sublimation. 4-inch soda lime glass wafers (University Wafer, 550 μm thick) were cleaned in a circulating 2% solution of Hellmanex III detergent heated to 50°C for 30 min followed by a high-pressure rinse with acetone and deionized water (DI). The wafers were then treated with O_2 plasma (Diener electronic GmbH, 200 W, 20 min). Immediately after, a 5 μm-thick parylene C layer was deposited via chemical vapor deposition (Diener electronic GmbH). The parylene C was then patterned by lithography and etching to produce 4 ×15 mm ribbons. This was done as follows: An aluminum reactive ion etching (RIE) hard mask was deposited through a stainless-steel shadow mask onto the parylene C wafer. The 80 nm layer of Al was evaporated in a PVD chamber in a vacuum of $< 2\times10^{-6}$ Torr using a rate of 5-15 Å/s. Parylene C was removed by RIE (200W, O_2 100 sccm). Finally, the Al mask was etched using a commercial wet etch solution. The parylene surface was then activated with O_2 plasma (50 W, 2 min), followed by vapor-phase treatment with 3-(mercaptopropyl)trimethoxysilane, MPTMS, by placing the samples in an MPTMS-vapor saturated chamber heated to 90 °C for 1 h. MPTMS treatment enhanced the adhesion of Au to the parylene C substrate. Next, a 10 nm-thick film of Au was thermally evaporated over the whole wafer in a vacuum of $< 2\times10^{-6}$ Torr using a rate of 3-5 Å/s. The organic pigment PN pixels were formed by thermal evaporation through a shadow mask at a base pressure of $< 2 \times 10^{-6}$ Torr using a rate of 0.1-0.5 nm/s. 30 nm of P-type H_2Pc and 30 nm of N-type PTCDI were successively deposited resulting in 60 nm total thickness of the organic layers (PN). It should be noted that efforts were made to produce semitransparent contacts from other materials, such as ITO. However, due to poor adhesion to the parylene substrate, approaches with ITO alone proved unsuccessful. Photothermal control samples were fabricated in the same way, except that instead of the PN layer, a 60 nm layer of indigo was thermally evaporated using the same conditions.

Optical tissue penetration modeling. Monte-Carlo light propagation simulation was conducted using the CUDAMCML software[51], a gpu-accelerated version of the well-established MCML software[50]. The tissue model consisted of three layers, a 1 mm layer of skin followed by 3 mm of subcutaneous adipose tissue and a 50 mm thick layer of muscle. Rat tissue optical parameters for all the wavelengths from Bashatkov and coworkers[52] were used. Light penetration was evaluated on a 0.1 mm vertical and radial mesh. 5 billion photons were used for each run of the simulation. The output files were convolved by the CONV software (a part of the MCML distribution), assuming a 2 mm FWHM diameter Gaussian light beam normalized to 700 mW of total power.

Photoelectrochemical characterization. Measurements of photovoltage and charging current of OEPC devices was performed according to previously described methods[46]. Briefly, the backside Au of the OEPC was contacted with a probe electrode connected to the positive terminal of an oscilloscope. Meanwhile, the negative terminal was connected to an Ag/AgCl electrode in 0.1 M KCl electrolyte, making contact to the top of the organic layer of the OEPC device. The droplet contact area was 0.126 cm^2. Pulsed illumination was provided by a 638 nm laser diode or a 660 nm high-power LED at various light intensities. Light intensity was verified using a calibrated Thorlabs Si PIN diode (Thorlabs SM1PD1B). The transient voltage change (V_t) was measured when the OEPC device was immersed in 0.1 M KCl, using a GeneClamp 500B amplifier (Axon Instruments) and a Digidata™ 1440A converter (Molecular Devices), as described previously[46]. It should be noted that the Ag/AgCl electrodes used in EPR measurements are illuminated, and that at the wavelengths of light used (638-660 nm) we do not observe any signal, artefact, or baseline shift related to illumination of the Ag/AgCl counter electrode. Overall, we have not found effects of photosensitivity of Ag/AgCl to wavelengths used in our work

Acute sciatic nerve stimulation. All animal experiments were approved by the institutional *Animal Care and Use Committee* of Columbia University Irving Medical Center. The implantations were carried out in Long Evans rats (200-250g at the time of implantation) that had no previous experimentation. Animals were housed in pairs, in a regular 12h/12h light/dark cycle and had access to food and water *ad libitum*.
Rats were anesthetized using 3% isoflurane and surgical site was shaved, disinfected and local analgesia was applied. A longitudinal incision (~1cm) along femoral axis was performed and the sciatic nerve was visualized. The connective tissue surrounding the nerve was minimally dissected to release and expose a longitudinal nerve section approximately 4mm long. OEPC devices were wrapped around the nerve, facing the PN pixel to the nerve surface, and fixed through adhesion of the parylene ribbon ends via capillary forces. 3 PN pixel diameter sizes (1, 1.4, and 3 mm) were tested. Tungsten microwires (diameter 50 μm) were placed in biceps femoris and plantar muscles, each providing a separate recording channel referenced to a microwire in the paraspinal subcutaneous tissue. CMAPs were recorded using a custom designed board based on an AD8237 differential amplifier chip and an RHD2000 board (Intan Technologies) for digitization. Illumination was provided by a 660 nm high-power LED (M660L4) with a collimator lens (SM2F32-B) controlled by a ThorLabs DC2200 High-Power LED. A minimum of 25 light pulses (3 s in between) was used for each light intensity/duration condition tested. CMAP amplitudes (maximal negative peak to maximal positive peak) were collected, and averaged, using a customized python code. Light intensity was verified with a Thorlabs SM1PD1B Si PIN diode. At the conclusion of the intra-operative recording session, the rats were euthanized. 5 rats were used for acute sciatic nerve experiments that aimed to characterize the performance of OEPC devices in regards of PN pixel size, light intensity, and light pulse duration.

Chronically implantable device fabrication. Clean 4" wafers were coated with 2.2 μm parylene C. The surface was then activated by an oxygen plasma treatment (50W, 120s) followed by physical vapor deposition of 1.5-2 μm thick layer of aluminum (vacuum $<1 \times 10^{-5}$ Torr, 20-30 nm/s) acting as mechanical support for the locking mechanism structures.

S1818 photoresist was spin coated on the substrates, exposed with MA6/BA6 Süss Mask Aligner and developed in MF-319. The aluminum layer was patterned using a commercial acidic etchant. The resist was stripped in acetone, followed by isopropanol and deionized water (DI). Propylene carbonate was then spin coated on the wafers at 2000 rpm and baked at 60˚C for 30s to act as an adhesion promoter[79] for the next 2.2 µm thick encapsulating layer of parylene C. The surface was then exposed to oxygen plasma (50W, 120s) and vapor treated with MPTMS in a closed chamber at 90˚C for 1h. The wafers were then washed with acetone, isopropanol and DI. Next, 10 nm of gold and a 30 nm of indium tin oxide (ITO) were sputtered onto the substrates. The sputtering target was In_2O_3/SnO_2 90/10 wt%, 99.99% pure (Lesker). Gold was deposited at 100 W, 3.4 mbar, 100% Ar, DC; ITO at 32 W, 4.5 mbar, 97% Ar, 3% O_2, RF. The outline of the implants was patterned using S1818 photoresist, MF-319 developer, ITO etchant (concentrated HCl), Au etchant (KI/I_2) and finally by RIE (200W, O_2 100 sccm). The wafer was washed in acetone, isopropanol and DI. A thin layer of 2% cleaning agent Micro90 was spin coated at 1000 rpm to act as an anti-adhesive layer before the next 2.2 µm thick sacrificial layer of parylene C. The openings for the photopixels were patterned by AZ 10XT resist, AZ developer and RIE (200W, O_2 100 sccm). The wafers were sequentially washed with acetone, isopropanol and DI. Then the protective layer of ITO was etched with concentrated HCl for a few seconds, followed by a quick wash in DI. Next, the organic pigments H_2Pc and PTCDI were evaporated from resistively heated crucibles at 1×10^{-6} Torr at rates of 1-6 Å/s to produce a 30/30 nm PN junction. Finally, the sacrificial parylene layer was peeled off to yield the patterned device. The wafer was rinsed with DI and tested using the EPR setup described above. In addition, control devices were subjected to an accelerated aging and light-stressing test according to the method described previously[47].

Chronic implantation test on the sciatic nerve. Rats were anesthetized and the sciatic nerve was exposed as previously described for acute stimulation. The CIP ribbon was passed behind the exposed sciatic nerve and the end of the ribbon was inserted through the ribbon loop using forceps. The PN pixel was placed facing the nerve surface, and the ribbon was pulled until the teeth passed through the ribbon loop, firmly closing the zip-tie mechanism. The ribbon was adjusted to fit snugly around the nerve without applying compressive force. The excess ribbon (~5mm) was then cut. Sutures were used to close the incision. After the operative procedure was complete, anesthesia was removed and the rats were allowed to recover from surgery. Triple antibiotic ointment and injectable analgesia were applied during the post-surgical recovery period.

The CMAP recording sessions were performed at 6, 18, 35, 56, 77, 96 and 103 days post-operatively (PO). Rats were anesthetized (3% isoflurane) and the implanted site was shaved to facilitate the attachment of EMG electrodes to the skin. Because multiple recording sessions were planned for each rat, we performed non-invasive CMAP monitoring to prevent ongoing disruption of muscle tissue. Gel electrodes (14 × 9 mm, Acuzone) were attached to the skin using Elefix conductive paste (Nihon Kohden). Electrodes were placed on the gastrocnemius and vastus lateralis (reference electrode) muscles, maintaining a consistent inter-electrode distance across sessions. Photostimulation was induced by a 638 nm laser diode with a maximum output power of 700 – 1200 mW driven by ThorLabs DC2200 High-Power LED controller. 250 light pulses (3s interpulse interval) with an intensity spanning 700 mW to 7 mW and duration from 1 ms to 0.05 ms were used. A

maximum power of 700 mW was used for all experiments up to 103 days, the higher range up to 1200 mW was tested at this point to try to maximize CMAP responses. Illumination point was approximately 2 cm far from the recording electrodes. CMAP signals were recorded as during the acute stimulation sessions. Video recordings of muscular twitches were performed.

Motor performance of the rats was evaluated in the immediate post-operative period and tested on an open field maze with horizontal and vertical obstacles at 53-54 days post-operatively. Walking and running gait, as well as ability to stand on hindlimbs and climb were observed.

In the subset of rats that showed responses after 103 days PO, the CMAPs were additionally recorded after creating an incision over the implantation site and opening the skin. Subsequently, photoinduced stimulation was repeated as per the above parameters after exposing the device to quantify device performance under maximal light intensity conditions.

At the end of the implantation period, the rats were euthanized, and the implanted sciatic nerve section was harvested and dissected. Additionally, the contralateral sciatic nerve anatomically corresponding to the implanted region was harvested for comparison. Gross pathological examination was performed for all harvested nerve segments. A total of 10 rats were chronically implanted with CIP devices.

Horizontal ladder test. The horizontal ladder rung apparatus had movable metal rungs (3 mm diameter), inserted between clear plexiglass side walls, and irregularly spaced at 2 or 4 cm. The rungs' position pattern was modified daily to prevent the animal from learning the pattern and thereby compensating for possible motor impairments. The animals were trained to cross the ladder over several sessions before recording and scoring the foot placement. The sessions were recorded using an Olympus E-M10 MII camera, positioned to optimally visualize foot placement. The hindlimb foot placement accuracy was visually analyzed frame-by-frame using a 7-category scale according to Metz et al.[71], from 0 (total miss) to 6 (correct placement). The start and the end of the ladder, as well as the steps before and after a gait interruption, were excluded from the analysis. Both groups of control (no surgery) and chronic OEPC implanted rats (tested 22 to 28 days after the implantation) were used for the study. The implanted rats were additionally subjected to a sham surgery in the contralateral sciatic nerve, which consisted of an equivalent incision in the *biceps femoris* muscle, dissection of tissue to visualize and mobilize sciatic nerve, and suturing for closure. The quantitative comparison of both hindlimbs was performed by averaging all the scores from each hindlimb placement across sessions and calculating the laterality index to determine whether there were any differences between performance of sham and OEPC-implanted limbs, defined as:

$$\frac{\text{mean sham score} - \text{mean implanted score}}{\text{mean sham score} + \text{mean implanted score}}$$

The statistical significance was calculated applying ANOVA with Bonferroni post hoc test.

Von Frey test. von Frey tests was carried out as per established guidelines in Chaplan et al.[72]. The rats were individually placed in bottom-opened cages on a wire mesh platform, in order to allow full access to the feet. After 30 min of accommodation, tactile allodynia was evaluated for both hindlimbs in the awake animals using von Frey hair filaments from

0.4 to 16 g (TouchTest kit, North Coast Medical). The filaments were placed perpendicular to the hindlimb plantar surface, avoiding the footpads, and a positive response was considered to be paw withdrawal or flinching. Filaments were tested when no ambulatory or grooming activities were observed, waiting several minutes between consecutive trials. Paw withdrawal 50% threshold response for both hindlimbs was measured using the up-down paradigm[72]. A group of rats subjected to previously described OEPC device implantation and contralateral sham surgeries (22 to 34 days post implantation), as well as a control group were tested. The 50% threshold response were averaged between different sessions for each hindlimb and the laterality index was calculated as previously described. The statistical significance was calculated applying ANOVA with Bonferroni post hoc test.

Immunohistochemistry. Rats were perfused with PFA 4% and both sciatic nerves were harvested, dissected, and post fixated in (PFA 4%, 4C, 12h). A nerve section immediately distal to the implanted device, and the equivalent section for the contralateral non-implanted sciatic nerve, were collected and included in agar (10%) blocks. Several transverse sections were obtained using a Leica VT1000S vibratome. The sections were subsequently washed in PBS 0.01 M and incubated in blocking solution (Donkey serum 10% and T-X100 0.3% in PBS, RT, 90 min). Next, the samples were incubated with primary antibody against neurofilament (BioLegend, 837904; 1:200) or against GFAP (Dako, Z0334; 1:300) in PBS with T-X100 0.3%, RT, o/n. Following several washes in PBS with T-X100 0.3%, the sections were incubated with the corresponding secondary antibody Alexa 488 or Alexa 594 (Invitrogen; 1:250 in PBS with T-X100 0.3%, RT, 3h). Finally, the samples were washed in PBS with T-X100 0.3%, incubated with DAPI (1:10000 in PBS with T-X100 0.3%, RT, 20min), washed again in PBS and mounted (Fluoromount Mounting Medium, Millipore-Sigma, F4680). Fluorescence images were obtained using an Echo Revolve or Zeiss LSM 800 microscope. The same acquisition parameters were used to obtain all the images for the same immunostaining of implanted and sham sciatic nerve samples. Echo Pro and ZEN 3.2 software were used for the images acquisition and the obtained images were processed using Image J. The number of immune-positive ROIs per area were measured and normalized to the respective sham samples values. The statistical significance was calculated applying Student's t-test.

Data Availability

All data supporting the results drawn from experiments can be found in the paper and supplementary information. Raw data used for the plots found in Figures 2-5, and S1-S2 are available from the authors upon request.

References

1. *Neuromodulation*. (Academic Press, 2009). Krames, Elliot S. Peckham, P. Hunter Rezai, Ali R.; eds. doi:10.1023/B:MYCO.0000003704.30293.b6
2. *Handbook of Bioelectronics*. (Cambridge University Press, 2015). Carrara, S., Iniewski, K.; eds. doi:10.1017/CBO9781139629539
3. Jastrzebska-Perfect, P. *et al.* Translational Neuroelectronics. *Adv. Funct. Mater.* **30**, 1909165 (2020).

4. Lozano, A. M. *et al.* Deep brain stimulation: current challenges and future directions. *Nat. Rev. Neurol.* **15**, 148–160 (2019).
5. Chuang, A. T., Margo, C. E. & Greenberg, P. B. Retinal implants: a systematic review. *Br. J. Ophthalmol.* **98**, 852–856 (2014).
6. Johnson, R. L. & Wilson, C. G. A review of vagus nerve stimulation as a therapeutic intervention. *J. Inflamm. Res.* **11**, 203–213 (2018).
7. Ben-Menachem, E., Revesz, D., Simon, B. J. & Silberstein, S. Surgically implanted and non-invasive vagus nerve stimulation: A review of efficacy, safety and tolerability. *Eur. J. Neurol.* **22**, 1260–1268 (2015).
8. Caravaca, A. S. *et al.* An Effective Method for Acute Vagus Nerve Stimulation in Experimental Inflammation. *Front. Neurosci.* **13**, 877 (2019).
9. Birmingham, K. *et al.* Bioelectronic medicines : a research roadmap. *Nat. Rev. Drug Discov.* **13**, 399–400 (2014).
10. Acarón Ledesma, H. *et al.* An atlas of nano-enabled neural interfaces. *Nat. Nanotechnol.* **14**, 645–657 (2019).
11. Tanabe, Y. *et al.* High-performance wireless powering for peripheral nerve neuromodulation systems. *PLoS One* **12**, e0186698 (2017).
12. Larson, C. E. & Meng, E. A review for the peripheral nerve interface designer. *J. Neurosci. Methods* **332**, 108523 (2020).
13. Thimot, J. & Shepard, K. L. Bioelectronic devices: Wirelessly powered implants. *Nat. Biomed. Eng.* **1**, 0051 (2017).
14. Agrawal, D. R. *et al.* Conformal phased surfaces for wireless powering of bioelectronic microdevices. *Nat. Biomed. Eng.* **1**, 0043 (2017).
15. Lee, B. *et al.* An Implantable Peripheral Nerve Recording and Stimulation System for Experiments on Freely Moving Animal Subjects. *Sci. Rep.* **8**, 6115 (2018).
16. Hernandez-Reynoso, A. G. *et al.* Miniature electroparticle-cuff for wireless peripheral neuromodulation. *J. Neural Eng.* **16**, 046002 (2019).
17. Amanda Singer, Benjamin Avants, Nishant Verma, Eric Lewis, Joshua C. Chen, Ariel K. Feldman, Shayok Dutta, Joshua Chu, John O'Malley, Michael Beierlein, Caleb Kemere, J. T. R. Magnetoelectric materials for miniature, wireless neural stimulation at therapeutic frequencies. *Neuron* **107**, 1–13 (2020).
18. Cotero, V. *et al.* Noninvasive sub-organ ultrasound stimulation for targeted neuromodulation. *Nat. Commun.* **10**, 952 (2019).
19. Piech, D. K. *et al.* A wireless millimetre-scale implantable neural stimulator with ultrasonically powered bidirectional communication. *Nat. Biomed. Eng.* **4**, 207–222 (2020).
20. Murakawa, K., Kobayashi, M., Nakamura, O. & Kawata, S. A wireless near-infrared energy system for medical implants. *IEEE Eng. Med. Biol.* **18**, 70–72 (1999).
21. Kim, J. *et al.* Active photonic wireless power transfer into live tissues. *Proc. Natl. Acad. Sci. U. S. A.* **117**, 16856–16863 (2020).
22. Jacques, S. L. Optical properties of biological tissues: A review. *Phys. Med. Biol.* **58**, 5007–5008 (2013).
23. Song, K. *et al.* Subdermal Flexible Solar Cell Arrays for Powering Medical Electronic Implants. *Adv. Healthc. Mater.* **5**, 1572–1580 (2016).
24. Haeberlin, A. *et al.* The first batteryless, solar-powered cardiac pacemaker. *Hear.*

Rhythm **12**, 1317–1323 (2015).
25. Abdo, A. *et al.* Floating light-activated microelectrical stimulators tested in the rat spinal cord. *J. Neural Eng.* **8**, (2011).
26. Yun, S. H. & Kwok, S. J. J. Light in diagnosis, therapy and surgery. *Nat. Biomed. Eng.* **1**, 0008 (2017).
27. Park, S. *et al.* Self-powered ultra-flexible electronics via nano-grating-patterned organic photovoltaics. *Nature* **561**, 516–521 (2018).
28. Jiang, Y. *et al.* Rational design of silicon structures for optically controlled multiscale biointerfaces. *Nat. Biomed. Eng.* **2**, 508–521 (2018).
29. Scanziani, M. & Häusser, M. Electrophysiology in the age of light. *Nature* **461**, 930–939 (2009).
30. Richter, C. P. & Tan, X. Photons and neurons. *Hear. Res.* **311**, 72–88 (2014).
31. Shapiro, M. G., Homma, K., Villarreal, S., Richter, C.-P. & Bezanilla, F. Infrared light excites cells by changing their electrical capacitance. *Nat. Commun.* **3**, 736 (2012).
32. Jiang, Y. *et al.* Heterogeneous silicon mesostructures for lipid-supported bioelectric interfaces. *Nat. Mater.* **15**, 1023–1030 (2016).
33. Jiang, Y. & Tian, B. Inorganic semiconductor biointerfaces. *Nat. Rev. Mater.* **3**, 473–490 (2018).
34. Jiang, Y. *et al.* Nongenetic optical neuromodulation with silicon-based materials. *Nat. Protoc.* **14**, 1339–1376 (2019).
35. Sytnyk, M. *et al.* Cellular interfaces with hydrogen-bonded organic semiconductor hierarchical nanocrystals. *Nat. Commun.* **8**, 91 (2017).
36. Martino, N. *et al.* Photothermal cellular stimulation in functional bio-polymer interfaces. *Sci. Rep.* **5**, 8911 (2015).
37. Wang, L. *et al.* Photovoltaic retinal prosthesis: implant fabrication and performance. *J. Neural Eng.* **9**, 046014 (2012).
38. Ferlauto, L. *et al.* Design and validation of a foldable and photovoltaic wide-field epiretinal prosthesis. *Nat. Commun.* **9**, 992 (2018).
39. Mathieson, K. *et al.* Photovoltaic retinal prosthesis with high pixel density. *Nat. Photonics* **6**, 391–397 (2012).
40. Prévot, P. H. *et al.* Behavioural responses to a photovoltaic subretinal prosthesis implanted in non-human primates. *Nat. Biomed. Eng.* **4**, 172–180 (2019).
41. Hopkins, J. *et al.* Photoactive Organic Substrates for Cell Stimulation: Progress and Perspectives. *Adv. Mater. Technol.* **1800744**, 1800744 (2019).
42. Di Maria, F., Lodola, F., Zucchetti, E., Benfenati, F. & Lanzani, G. The evolution of artificial light actuators in living systems: from planar to nanostructured interfaces. *Chem. Soc. Rev.* (2018). doi:10.1039/C7CS00860K
43. Sytnyk, M. *et al.* Hydrogen-Bonded Organic Semiconductor Micro- And Nanocrystals: From Colloidal Syntheses to (Opto-)Electronic Devices. *J. Am. Chem. Soc.* **136**, 16522−16532 (2014).
44. Hunger, K. Toxicology and toxicological testing of colorants. *Rev. Prog. Color. Relat. Top.* **35**, 76–89 (2005).
45. Rand, D. *et al.* Direct Electrical Neurostimulation with Organic Pigment Photocapacitors. *Adv. Mater.* **30**, 1707292 (2018).
46. Jakešová, M. *et al.* Optoelectronic control of single cells using organic

photocapacitors. *Sci. Adv.* **5**, eaav5265 (2019).
47. Ejneby, M. S. *et al.* Extracellular Photovoltage Clamp Using Conducting Polymer-Modified Organic Photocapacitors. *Adv. Mater. Technol.* **5**, 1900860 (2020).
48. *Electromyography Physiology, Engineering, and noninvasive applications*. (John Wiley & Sons, 2004).
49. Fortin, J. B. & Lu, T.-M. *Chemical Vapor Polymerization, The Growth and Properties of Parylene*. (Springer Science+Business Media, 2004).
50. Jacques, S. L. & Wang, L. MCML - Monte Carlo Modeling of Light Transport in Tissues. *Comput. Methods Programs Biomed.* **47**, 131–146 (1995).
51. Alerstam, E., Svensson, T. & Andersson-Engels, S. Parallel computing with graphics processing units for high-speed Monte Carlo simulation of photon migration. *J. Biomed. Opt.* **13**, 060504 (2008).
52. Bashkatov, A. N., Genina, E. A. & Tuchin, V. V. Optical properties of skin, subcutaneous, and muscle tissues: A review. *J. Innov. Opt. Health Sci.* **4**, 9–38 (2011).
53. LIA. *American National Standard for Safe Use of Lasers*. *Laser Institute of America* **ANSI Z136.**, (2007).
54. Cogan, S. F. Neural Stimulation and Recording Electrodes. *Annu. Rev. Biomed. Eng.* **10**, 275–309 (2008).
55. Boehler, C., Carli, S., Fadiga, L., Stieglitz, T. & Asplund, M. Tutorial: guidelines for standardized performance tests for electrodes intended for neural interfaces and bioelectronics. *Nat. Protoc.* **15**, 3557–3578 (2020).
56. Đerek, V., Rand, D., Migliaccio, L., Hanein, Y. & Głowacki, E. D. Untangling Photofaradaic and Photocapacitive Effects in Organic Optoelectronic Stimulation Devices. *Front. Bioeng. Biotechnol.* **8**, 284 (2020).
57. Merrill, D. R., Bikson, M. & Jefferys, J. G. R. Electrical stimulation of excitable tissue: Design of efficacious and safe protocols. *J. Neurosci. Methods* **141**, 171–198 (2005).
58. Harnack, D. *et al.* The effects of electrode material, charge density and stimulation duration on the safety of high-frequency stimulation of the subthalamic nucleus in rats. *J. Neurosci. Methods* **138**, 207–216 (2004).
59. Schoen, I. & Fromherz, P. Activation of Na+ channels in cell membrane by capacitive stimulation with silicon chip. *Appl. Phys. Lett.* **87**, 193901–193903 (2005).
60. Seixas de Melo, J. *et al.* Photophysics of an indigo derivative (keto and leuco structures) with singular properties. *J. Phys. Chem. A* **110**, 13653–13661 (2006).
61. Jeppesen, C., Mortensen, N. A. & Kristensen, A. The effect of Ti and ITO adhesion layers on gold split-ring resonators. *Appl. Phys. Lett.* **97**, 2012–2015 (2010).
62. Benck, J. D., Pinaud, B. A., Gorlin, Y. & Jaramillo, T. F. Substrate selection for fundamental studies of electrocatalysts and photoelectrodes: Inert potential windows in acidic, neutral, and basic electrolyte. *PLoS One* **9**, e107942 (2014).
63. Matarese, B., Mello, J. C. De, Feyen, P., Benfenati, F. & Preparation, A. S. Investigation of the stability and biocompatibility of commonly used electrode materials in organic neuro- optoelectronics. 1539–1542 (2015).
64. Selvakumaran, J., Hughes, M. P., Ewins, D. J. & Richards, P. R. Biocompatibility

studies of materials used for chronically implantable microelectrodes. *1st Annu. Int. IEEE-EMBS Spec. Top. Conf. Microtechnologies Med. Biol. - Proc.* 521–525 (2000). doi:10.1109/MMB.2000.893839

65. Ilic, B. & Craighead, H. G. Topographical patterning of chemically sensitive biological materials using a polymer-based dry lift off. *Biomed. Microdevices* **2**, 317–322 (2000).
66. Yu, H., Xiong, W., Zhang, H., Wang, W. & Li, Z. A cable-tie-type parylene cuff electrode for peripheral nerve interfaces. *Proc. IEEE Int. Conf. Micro Electro Mech. Syst.* 9–12 (2014). doi:10.1109/MEMSYS.2014.6765560
67. Cobo, A. M. *et al.* Parylene-Based Cuff Electrode With Integrated Microfluidics for Peripheral Nerve Recording, Stimulation, and Drug Delivery. *J. Microelectromechanical Syst.* **28**, 36–49 (2019).
68. Günter, C., Delbeke, J. & Ortiz-Catalan, M. Safety of long-term electrical peripheral nerve stimulation: Review of the state of the art. *J. Neuroeng. Rehabil.* **16**, 13 (2019).
69. Ayaz, M. *et al.* Sexual dependency of rat sciatic nerve fiber conduction velocity distributions. *Int. J. Neurosci.* **117**, 1537–1549 (2007).
70. Koo, Y. S., Cho, C. S. & Kim, B. J. Pitfalls in using electrophysiological studies to diagnose neuromuscular disorders. *J. Clin. Neurol.* **8**, 1–14 (2012).
71. Metz, G. A. & Whishaw, I. Q. The ladder rung walking task: A scoring system and its practical application. *J. Vis. Exp.* **28**, 1204 (2009).
72. Chaplan, S. R., Bach, F. W., Pogrel, J. W., Chung, J. M. & Yaksh, T. L. Quantitative assessment of tactile allodynia in the rat paw. *J. Neurosci. Methods* **53**, 55–63 (1994).
73. Cameron, T. Safety and efficacy of spinal cord stimulation for the treatment of chronic pain: A 20-year literature review. *J. Neurosurg.* **100**, 254–267 (2004).
74. Perryman, L. T. Spinal Cord Stimulation Costs and Complications can be reduced by Wireless Nanotechnology. A Review of Traditional Equipment Expenses Compared to Wireless Stimulation. *Am. J. Anesth. Clin. Res.* **4**, 19–24 (2018).
75. Krook-Magnuson, E., Gelinas, J. N., Soltesz, I. & Buzsáki, G. Neuroelectronics and biooptics: Closed-loop technologies in neurological disorders. *JAMA Neurol.* **72**, 823–829 (2015).
76. Edwards, C. A., Kouzani, A., Lee, K. H. & Ross, E. K. Neurostimulation Devices for the Treatment of Neurologic Disorders. *Mayo Clin. Proc.* **92**, 1427–1444 (2017).
77. Gutruf, P., Good, C. H. & Rogers, J. A. Perspective: Implantable optical systems for neuroscience research in behaving animal models—Current approaches and future directions. *APL Photonics* **3**, 120901 (2018).
78. Lu, L. *et al.* Wireless optoelectronic photometers for monitoring neuronal dynamics in the deep brain. *Proc. Natl. Acad. Sci. U. S. A.* **115**, E1374–E1383 (2018).
79. Chang, J. H.-C., Lu, B. & Tai, Y.-C. Adhesion-enhancing surface treatments for parylene deposition. *16th Int. Solid-State Sensors, Actuators Microsystems Conf.* 390–393 (2011).

Author Contributions
M.S.E.; M.J.; J.J.F.; and L.M. contributed equally to this manuscript. M.S.E.; M.J.; and L.M. carried out the photoelectrochemical characterizations. M.S.E.; M.J., V.Đ.; D.K.; J.G. performed acute experiments and analyzed data. L.M. fabricated devices for acute experiments. M.J. fabricated devices for chronic experiments. V.Đ. wrote programs for data acquisition, processing, and MC modeling. I.S. performed calculations with finite element models. Z.Z. designed and developed the electrophysiological acquisition hardware. J.J.F.; D.K.; and J.G. performed the rodent surgeries. Chronic data was collected and analyzed by M.J.; J.J.F.; Z.Z.; J.G.; and E.D.G. J.J.F. and M.S.E. performed the rat behavioral testing. J.J.F. conducted immunohistochemistry experiments. The project was led and supervised by M.B.; D.K., V.Đ.; J.G.; E.D.G. The manuscript was written with input from all coauthors.

Acknowledgements
This project has received funding from the European Research Council (ERC) under the European Union's Horizon 2020 research and innovation program (grant agreement No. 949191). The authors gratefully acknowledge financial support from the Knut and Alice Wallenberg Foundation within the framework of the Wallenberg Centre for Molecular Medicine at Linköping University, the Swedish Research Council (Vetenskapsrådet, 2018-04505), and the Swedish Foundation for Strategic Research (SSF). This work has been supported in part by Croatian Science Foundation under the project UIP-2019-04-1753. This work was also supported by Columbia University, School of Engineering and Applied Science; as well as Columbia University Medical Center, Department of Neurology and Institute for Genomic Medicine.

Author information
Malin Silverå Ejneby, Marie Jakešová, Jose J. Ferrero, and Ludovico Migliaccio all contributed equally to this manuscript.

Competing Interests
The authors declare no conflicts of interest.

Supplementary Information
The *supplementary information* file contains additional figures S1-S5, an appendix describing the photothermal heating model, and captions for the supplementary videos 1-4.

Nature Biomedical Engineering **volume 6**, pages741–753 (2022)

Supplementary information for:

A chronic photocapacitor implant for minimally invasive neurostimulation with deep-red light

Malin Silverå Ejneby, Marie Jakešová, Jose J. Ferrero, Ludovico Migliaccio, Ihor Sahalianov, Zifang Zhao, Magnus Berggren, Dion Khodagholy, Vedran Đerek,* Jennifer Gelinas,* Eric Daniel Głowacki*

Supplementary Videos 1-4 captions:

Video 1 | Video of the initial acute photostimulation experiments as described in Figure 3. Illumination pulses are modulated at a frequency of 1 Hz, and the experimenter places his hand in the beam in order to block illumination to show that stimulation only occurs when the light reaches the implanted OEPC device.

Video 2 | This video corresponds to experiments shown in Figure 5. At 14 days following implantation of the CIP device, 1-ms light impulses are modulated at a frequency of 0.33 Hz, demonstrating clearly leg muscle twitches. The muscle twitches are observable at 3 second intervals, however the actual red light is not always perceptible to the viewer. This is due to the difficulty, even with relatively high video frame rate, for the digital camera CCD to capture the 1 millisecond impulses.

Video 3 | This video corresponds to the datapoint at 103 days in Figure S2. When the implant site is surgically opened and photostimulation is performed, clear muscle twitches are once again visible.

Video 4 | Horizontal ladder test for implanted versus control rats.

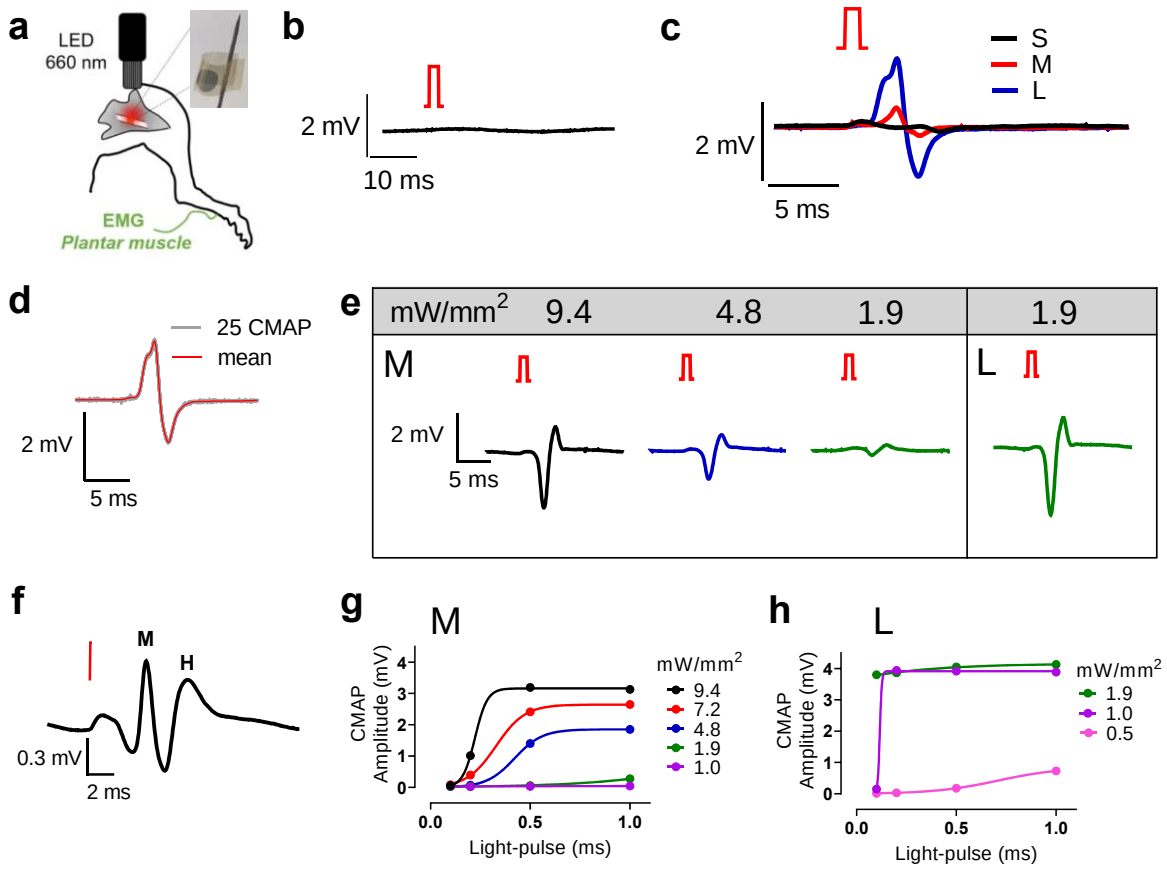

Figure S1. | Acute sciatic nerve photostimulation registered in the Plantar muscle. a, Schematic of the sciatic nerve stimulation experiment design for acute conditions, with inset photograph showing a free-standing device prior to implantation and EMG electrode inserted into the plantar muscle **b,** Illumination of a sham device, without the PN pixel (only gold on parylene C) gives no response or artefact. 1-ms light-pulses, 8.1 mW/mm^2 irradiation. **c,** Averaged evoked CMAPs in the plantar muscle (Rat #1) during 25 repetitive light-pulse stimulation (1 ms, 9.4 mW/mm^2 irradiation, 3 seconds in-between), for the respectively-sized OEPC devices. **d,** Highly reproducible repeated stimulation can be evidenced when 25 CMAPs are plotted on top of each other (in grey) for biceps femoris after repetitive stimulation with a M-sized OEPC device (Rat #1). 1-ms light-pulses, 9.4 mW/mm^2 irradiation, 3 seconds in-between. The averaged response is shown in red. **e,** Examples of CMAPs evoked at different light intensities, 1 ms pulses on M- and L-sized OEPC devices (Rat #2) **f,** Average response demonstrating CMAP with M and H wave when relatively low charge is injected using the medium-sized device (n = 25 responses, intensity 7.2 mW/mm^2 pulse duration 0.2 ms). **g**, Average plantar muscle CMAP amplitudes versus light-pulse length, at different light intensities. M-sized OEPC device. 25 pulses, 3 seconds in-between, for each condition. **h,** Average plantar muscle CMAP amplitudes versus light-pulse length, at different light intensities. L-sized OEPC device. 25 pulses, 3 seconds in-between, for each condition. CMAP amplitude saturates at lower intensities and pulse times for the L device compared with the M device.

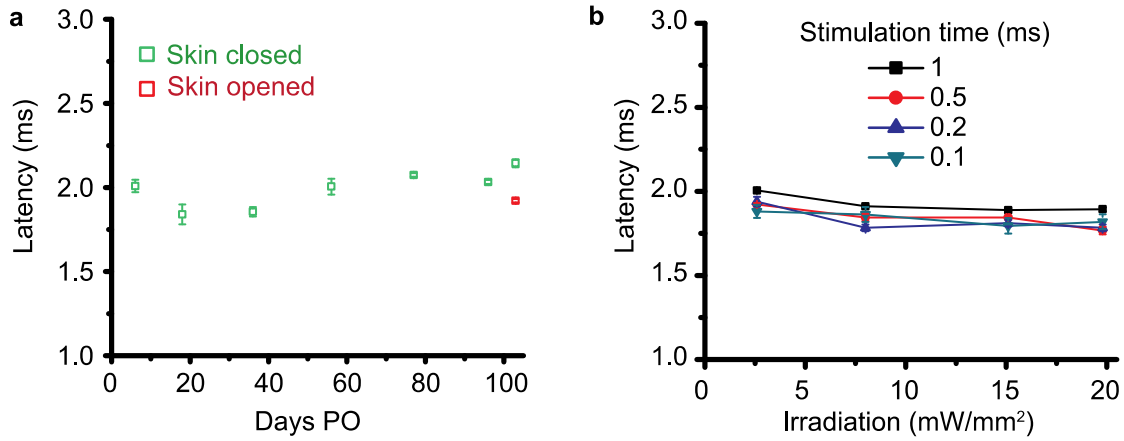

Figure S2. | CMAP latency depends on stimulation strength. a, CMAP latency over implantation period for a sample rat. Note that although CMAP latency increases after 60 days (green data points), this change is reversible by increasing light intensity through opening of skin superficial to CIP implantation site (red data point). This indicates that the apparent increase in latency is due to drop in device performance rather than detriment to the nerve. **b,** CMAP latency is reduced by increasing light intensity, further confirming that at long implantation times, device performance deterioration is connected with latency rise.

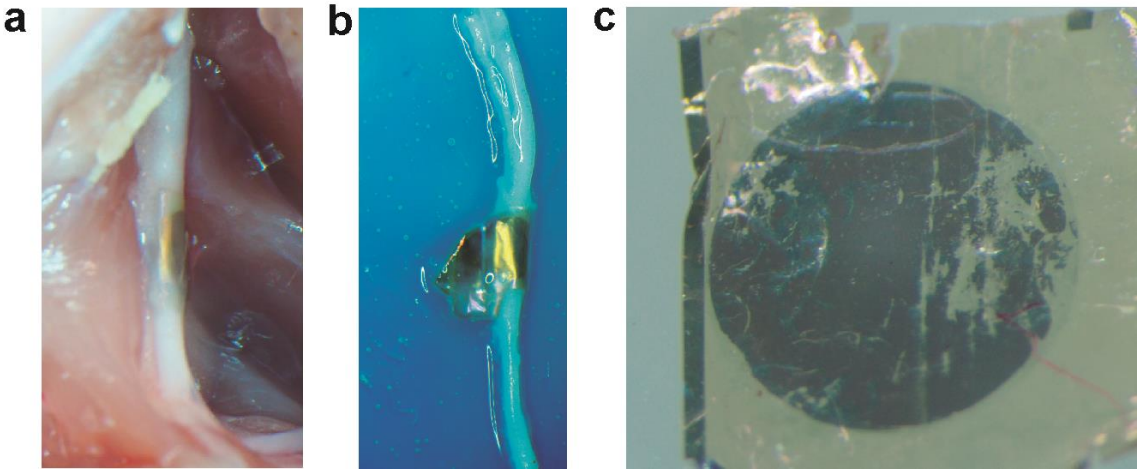

Figure S3. | CIP explantation. a, b, CIP affixed to a perfused rat's sciatic nerve before and after harvest of the nerve (69 days post-implantation) **c,** Micrograph of the organic PN pigment layers from the explanted CIP device showing focal points of delamination of the organic semiconductor layers. The ITO-capped Au remains visually intact.

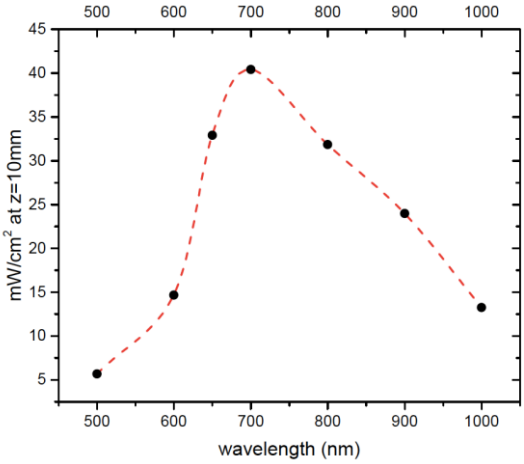

Figure S4. | Wavelength dependence of optical power transmission through tissue. Intensity at a fixed depth of z=10 mm below the skin, calculated as a function of beam wavelength. A window between 650 – 800 nm affords the most optimal transmissivity through skin/fat/muscle tissue. The dark circles are points calculated based on available data parameters, while the red dashed line is a guide for the eye.

Supplementary Appendix 1. Calculation of photothermal heating

Deep-red light laser stimulation can potentially cause damage to the tissue via heating. Laser heating is compensated by natural cooling processes, such as convectional cooling of the skin and tissue cooling by blood flow. This process can be estimated by solving the heat transfer partial differential equation with the finite element method.

Rat tissue simulation geometry consisted of three domains, assembled in a rectangular shape with surface area 20 × 20 = 400 mm^2. The thicknesses of the layers were: 1 mm of skin, 3 mm of fat, and 10 mm of muscle, as depicted in Figure S5a.

Simulation of the laser-induced heating of the rat tissue was performed using a modified heat transfer equation

$$\rho C_p \frac{\partial T}{\partial t} + \nabla \cdot \mathbf{q} = Q + Q_{bio} \quad (1)$$

where ρ — the density of tissue, C_p—specific heat capacitance of tissue at constant pressure, $\mathbf{q}$ is a heat flux, and Q represents heat sources (laser beam). According to the Fourier's law, heat flux $\mathbf{q}$ is proportional to the temperature gradient and thermal conductivity k

$$\mathbf{q} = -k\nabla T \quad (2)$$

Pennes approximation [1] was used to describe biological aspects of the heat transfer, such as the impact of blood flow and metabolic heating

$$Q_{bio} = \rho_b C_{p,b} \omega_b (T_b - T) + Q_{met} \quad (3)$$

where ρ_b — the density of blood, $C_{p,b}$—specific heat capacitance of blood at constant pressure, ω_b— blood volumetric perfusion rate, $T_b = 36$℃— arterial blood temperature, and Q_{met}— metabolic heat source. Representation of the blood perfusion in equation (3) is valid for the case of a complex of small blood vessels, uniformly distributed in tissue. Large blood vessels were omitted during the simulations. Under such conditions, cooling is represented by the isotropic heat dissipation across the simulation domains.

An additional source of cooling is a convective heat transfer on the border between skin and air. It was described as a boundary condition on the top of the skin domain with a heat flux

$$q_0 = h(T_{exp} - T) \quad (4)$$

where h is a heat transfer coefficient, and $T_{exp} = 20$ ℃ is the temperature outside of a tissue. All other boundary conditions were set to thermal insulation (Figure S5a)

Each of the domains (skin, fat, and muscle) has its own set of parameters ρ, k, C_p, Q_{met}, and ω_b, listed in table S1. Other simulation parameters, used for the description of arterial blood and convective heat transfer coefficient of the skin, also can be found in table S1.

The shape of the laser beam inside the tissue was simulated from the Monte-Carlo data, depicted in Figure 1f. The integration of the Monte-Carlo data inside the tissue gives a total laser power of 0.57 W, close to the initial 0.7 W beam after reflection and absorption. Distribution of the beam was represented with a Gaussian function, which captures intense photonic scattering inside the tissue with an account of different absorption and scattering coefficients in skin, fat, and muscle layers

$$Q(x,y,z) = \frac{2Q_0}{(2\pi)^{3/2}\sigma_x\sigma_y\sigma_z} e^{-\left(\frac{x^2}{2\sigma_x^2}+\frac{y^2}{2\sigma_y^2}+\frac{z^2}{2\sigma_z^2}\right)} \quad (5)$$

where Q_0=0.57 W is a total laser power inside the tissue, and dispersion values were adopted from the fitting of data in Figure 1f and depicted in Figure S5b,c, $\sigma_x = \sigma_y = 0.156$ cm, and $\sigma_z = 0.13$ cm.

All simulations were performed with the COMSOL software package [8].

As a first step, the simulation of the tissue without a laser beam was conducted. A stationary temperature map can be found in Figure S5d. Under stationary conditions, heat dissipation from the skin's surface is compensated by the metabolic heating and heating from the blood flow, which creates a minor temperature gradient. The temperature has a minimum on top of the skin and further increases towards 36 ℃ deep in the rat body. Stationary temperature on top of each of domains after the simulations: $T_{stat,skin}$ = 34.02 ℃, $T_{stat,fat}$ = 34.17 ℃, $T_{stat,muscle}$ = 34.77 ℃.

The laser beam spreads uniformly with a relatively large dispersion and can transmit several mm deep into the tissue. There are no points on the skin where laser intensity is much higher than anywhere else due to photonic scattering. All simulations of laser heating were carried with the initial stationary temperature distribution (Figure S5d). Temperature maps of the tissue after 1 ms and 1 s of heating are in (Figure S5e,f). For an exact comparison, data is depicted at the same temperature range from 34 ℃ to 42 ℃. After the 1 ms laser pulse, there are no noticeable differences in the temperature, even at the central laser incidence point. After 1s of laser heating, there is an apparent region with increased temperature, spreading across skin and fat domains but not the muscle. What is essential, even after 1s of heating, there are no regions with a temperature higher than 42 ℃.

As for short laser 1 ms pulse, which was used during the experiments, its impact on the temperature is in Figure S5g. The temperature increase after the laser pulse directly under the beam center on top of the skin is only 0.0053 ℃. A similar increase in 0.00517 ℃ was recorded on top of the fat domain. A short duration of heating can explain such a minor increase in temperature. The tissue cooling (inset in Figure S5g) after 1 ms pulse is much slower because of a small temperature gradient. Heat dissipation occurs via convection on top of the skin layer and diffusion of heat from the fat layer to muscle one. The temperature decreases in the skin and fat layers and slightly increases on top of the muscle layer after 20 s of cooling.

As for much longer pulses (which is not the case in the current paper), rat tissue was exposed at a constant laser heating for 10 s. The corresponded temperature increase in the spatial points, located under the laser center on top of skin, fat, and muscle domains, are in Figure S5h. Tissue temperature reaches dangerous values of more than 42 ℃ only after 1 s of constant heating.

To sum up this section, we performed finite element method simulations of a heat transfer in rat tissue under laser exposure. Simulations of a 1 ms laser pulse (as was used in the experiments here) cause almost no effect on the temperature (an increase of temperature is ≈ 0.005 ℃ on top of skin and fat, directly under the beam incidence). Although lasers with such power and

wavelength can be harmful after long-term exposures of more than 1s, short 1 ms pulses are demonstrated to be completely safe.

1) Harry H. Pennes, Analysis of Tissue and Arterial Blood Temperatures in the Resting Human Forearm, Journal of Applied Physiology, Vol. 1 no. 2, pp. 93-122, 1 August 1948.
2) Pop, M., Molckovsky, A., Chin, L., Kolios, M. C., Jewett, M. A., & Sherar, M. D. (2003). Changes in dielectric properties at 460 kHz of kidney and fat during heating: importance for radio-frequency thermal therapy. *Physics in Medicine & Biology*, *48*(15), 2509.
3) P.A. Hasgall, F. Di Gennaro, C. Baumgartner, E. Neufeld, M.C. Gosselin, D. Payne, A. Klingenböck, and N. Kuster, IT'IS Database for thermal and electromagnetic parameters of biological tissues, Version 3.0, 2015. www.itis.ethz.ch/database.
4) Xu, F., Seffen, K. A., & Lu, T. J. (2008). Temperature-Dependent Mechanical Behaviors of Skin Tissue. *IAENG International Journal of Computer Science*, *35*(1).
5) De Dear, R. J., Arens, E., Hui, Z., & Oguro, M. (1997). Convective and radiative heat transfer coefficients for individual human body segments. *International Journal of Biometeorology*, *40*(3), 141-156.
6) Ricketts, P. L., Mudaliar, A. V., Ellis, B. E., Pullins, C. A., Meyers, L. A., Lanz, O. I., ... & Diller, T. E. (2008). Non-invasive blood perfusion measurements using a combined temperature and heat flux surface probe. *International journal of heat and mass transfer*, *51*(23-24), 5740-5748.
7) Simpson, C. R., Kohl, M., Essenpreis, M., & Cope, M. (1998). Near-infrared optical properties of ex vivo human skin and subcutaneous tissues measured using the Monte Carlo inversion technique. *Physics in Medicine & Biology*, *43*(9), 2465.
8) COMSOL Multiphysics® v. 5.5. COMSOL AB: Stockholm, Sweden.

Table S1. Parameters of the heat transfer model.

	ρ $\mathrm{kg/m^3}$	k $\mathrm{W/(m \cdot K)}$	C_p $\mathrm{J/(kg \cdot K)}$	Q_{met} $\mathrm{W/m^3}$	ω_b $1/\mathrm{s}$
Skin [3,4,7]	1109	0.37	3391	1827	0.002
Fat [2,3,7]	911	0.21	2348	465	0.0005
Muscle [3,7]	1090	0.49	3421	1052	0.0007
	ρ_b $\mathrm{kg/m^3}$	T_b ℃	$C_{p,b}$ $\mathrm{J/(kg \cdot K)}$		
Blood [3,6]	1050	36	3617		
	h $W/(\mathrm{m^2 \cdot K})$				
Skin [5]	4.5				

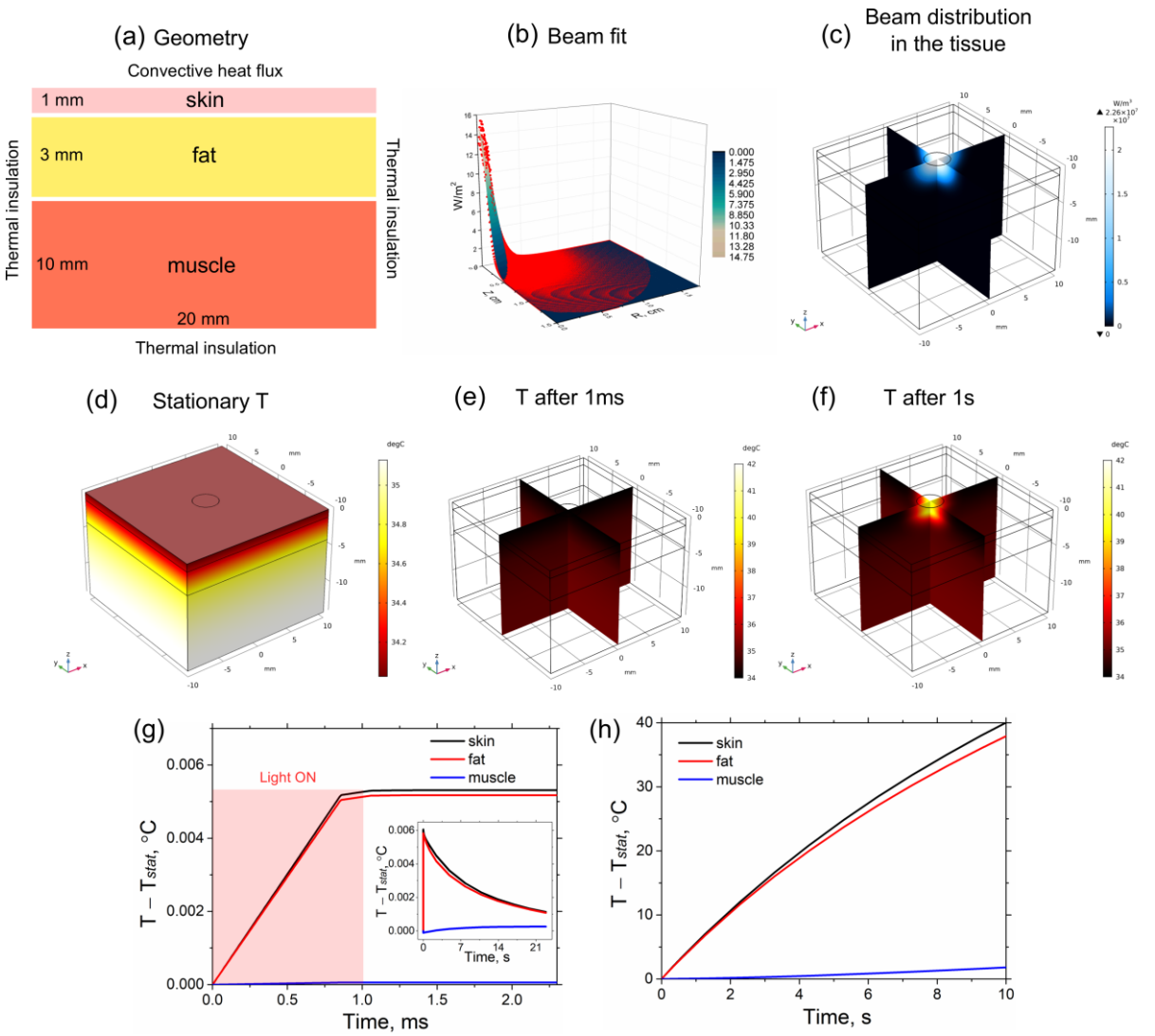

Figure S5. (a) Geometry description and boundary conditions of a rat tissue (note that 3D geometry was simulated). (b) Fitting of the Monte-Carlo data, adopted from Figure 1f, red dots represent Monte-Carlo data points, and the surface represents the Gaussian fit with $\sigma_r = 0.156$ cm and $\sigma_z = 0.13$ cm. (c) Gaussian fit of the laser beam distribution inside the rat tissue. (d) stationary temperature distribution across the rat tissue without laser exposure. (e),(f) temperature distribution across the rat tissue under a laser exposure for 1 ms or 1 s with the common color map and legend. (g) An increase of temperature (T - T_{stat}) as a function of time in the points located under the laser beam on top of the skin, fat, and muscle layers after a 1ms pulse. Inset in (g) shows the cooling of tissue for 20 s after 1 ms laser pulse heating. (h) An increase of temperature (T - T_{stat}) during 10 s constant laser heating.